Geophysical Journal International

Geophys. J. Int. (2018) **212,** 189–210
Advance Access publication 2017 September 22
GJI Rock and mineral physics, rheology

doi: 10.1093/gji/ggx392

Stress-dependent elastic properties of shales—laboratory experiments at seismic and ultrasonic frequencies

Dawid Szewczyk,[1] Andreas Bauer[1,2] and Rune M. Holt[1]

[1] *Faculty of Engineering, Department of Geoscience and Petroleum, Norwegian University of Science and Technology (NTNU),* 7491 *Trondheim, Norway. E-mail: dawid.szewczyk@ntnu.no*
[2] *SINTEF Petroleum Research, Formation Physics,* 7465 *Trondheim, Norway*

Accepted 2017 September 18. Received 2017 September 13; in original form 2017 March 30

SUMMARY

Knowledge about the stress sensitivity of elastic properties and velocities of shales is important for the interpretation of seismic time-lapse data taken as part of reservoir and caprock surveillance of both unconventional and conventional oil and gas fields (e.g. during 4-D monitoring of CO_2 storage). Rock physics models are often developed based on laboratory measurements at ultrasonic frequencies. However, as shown previously, shales exhibit large seismic dispersion, and it is possible that stress sensitivities of velocities are also frequency dependent. In this work, we report on a series of seismic and ultrasonic laboratory tests in which the stress sensitivity of elastic properties of Mancos shale and Pierre shale I were investigated. The shales were tested at different water saturations. Dynamic rock engineering parameters and elastic wave velocities were examined on core plugs exposed to isotropic loading. Experiments were carried out in an apparatus allowing for static-compaction and dynamic measurements at seismic and ultrasonic frequencies within single test. For both shale types, we present and discuss experimental results that demonstrate dispersion and stress sensitivity of the rock stiffness, as well as *P*- and *S*-wave velocities, and stiffness anisotropy. Our experimental results show that the stress-sensitivity of shales is different at seismic and ultrasonic frequencies, which can be linked with simultaneously occurring changes in the dispersion with applied stress. Measured stress sensitivity of elastic properties for relatively dry samples was higher at seismic frequencies however, the increasing saturation of shales decreases the difference between seismic and ultrasonic stress-sensitivities, and for moist samples stress-sensitivity is higher at ultrasonic frequencies. Simultaneously, the increased saturation highly increases the dispersion in shales. We have also found that the stress-sensitivity is highly anisotropic in both shales and that in some of the cases higher stress-sensitivity of elastic properties can be seen in the direction parallel to the bedding plane.

Key words: Elasticity and anelasticity; Geomechanics; Acoustic properties; Seismic anisotropy.

1 INTRODUCTION

Shale is the main constituent of the overburden of conventional hydrocarbon reservoirs. As such, it has a strong influence on seismic waves recorded during the surveys. In particular, with the use of time-lapse seismic, it has become feasible to detect changes in seismic travel time that can be linked to stress changes induced by depletion or inflation of a reservoir beneath (e.g. Kenter *et al.* 2004; Barkved & Kristiansen 2005; Hatchell & Bourne 2005; Røste *et al.* 2006). Shale characterization is also required for addressing cap rock integrity and assessment of borehole stability during drilling operations. In addition, with the developments of gas and oil shales, shale data is required as part of reservoir characterization. There is a solid base of papers in the literature that address static and ultrasonic elastic properties of shales (e.g. Kaarsberg 1959; Jones & Wang 1981; Johnston 1987; Vernik & Nur 1992; Johnston & Christensen 1995; Hornby 1998; Suarez-Rivera *et al.* 2001; Domnesteanu *et al.* 2002; Wang 2002; Duranti *et al.* 2005; Dewhurst & Siggins 2006; Deng *et al.* 2009; Sarker & Batzle 2010; Dewhurst *et al.* 2011; Piane *et al.* 2014; Sarout *et al.* 2014a; Bauer *et al.* 2015; Mikhaltsevitch *et al.* 2016; Keller 2017). It is known that fluid saturated crustal rocks are elastically deformable and dispersive in nature (e.g. Nur & Byerlee 1971; Zimmerman 1991), and several models describing the interplay between the fluid and the solid phases of the rock as a source of dispersion have been proposed (e.g. Biot 1956; White *et al.* 1975; Mavko & Nur 1979; Mavko & Jizba 1991; Dvorkin & Nur 1993; Gurevich & Lopatnikov 1995; Chapman 2003; Pride & Berryman

Table 1. List of sample orientations, saturants used for RH control during stabilization in desiccators, corresponding relative humidity, saturation of the sample, and volume change during stabilization for the tested samples.

No. of sample	Shale	Orientation with respect respect to symmetry axis	Saturant used for RH control	RH theoretical (RH measured) (per cent)	Saturation	Change of volume during stabilization (per cent)
S 01	Mancos	0°	as received	–	0.72 ± 0.05	0
S 02	Mancos	45°	as received	–	0.72 ± 0.05	0
S 03	Mancos	90°	as received	–	0.72 ± 0.05	0
S 04	Pierre I	0°	LiCl	11.3 (18.9)	0.10 ± 0.06	–3,59
S 05	Pierre I	45°	LiCl	11.3 (18.9)	0.10 ± 0.06	–4,34
S 06	Pierre I	90°	LiCl	11.3 (18.9)	0.10 ± 0.06	–3,13
S 07	Pierre I	0°	$MgCl_2$	32.9 (33.9)	0.23 ± 0.05	–3,10
S 08	Pierre I	0°	$Mg(NO_3)_2$	54.4 (55.1)	0.48 ± 0.03	–3,18
S 09	Pierre I	45°	$Mg(NO_3)_2$	54.4 (55.1)	0.48 ± 0.03	–2,42
S 10	Pierre I	90°	$Mg(NO_3)_2$	54.4 (55.1)	0.48 ± 0.03	–5,79
S 11	Pierre I	0°	NaCl	75.4 (76)	0.70 ± 0.02	–3,16

2003a,b; Chapman *et al.*, 2006; Muller & Gurevich 2006; Gurevich *et al.* 2010; Gueguen & Sarout 2011). Although techniques allowing for measuring elastic wave velocities and attenuation at different frequency ranges are available (e.g. Winkler & Nur 1979; Spencer 1981), only few groups report on dispersion measurements (e.g. Jackson & Paterson 1993; Batzle *et al.* 2001; Zadler *et al.* 2004; Duranti *et al.* 2005; Priest *et al.* 2005; Lucet & Zinszner 2006; Tisato & Madonna 2012; Nakagawa *et al.* 2013; Delle McCann *et al.* 2014; Mikhaltsevitch *et al.* 2014; Piane *et al.* 2014; Pimienta *et al.* 2015; Zhao *et al.* 2015; Szewczyk *et al.* 2016). As a consequence, descriptions of seismic dispersion often remain theoretical and require experimental verification (Müller *et al.* 2010). During production, reservoir and overburden formations undergo continuous stress changes, and understanding the influence of stress on the dispersive rock properties is essential for optimizing the productivity and assuring safety of field operations. Therefore, laboratory studies performed at various frequency ranges are of great value. It has been also shown that the ultrasonic stress sensitivity of velocities in shales depend strongly on applied stress path (Holt *et al.* 2016), as such laboratory studies should be executed under well-defined conditions.

In this work, we report on a series of laboratory experiments addressing the influence of isotropic stress change on dispersive properties of Mancos shale and Pierre shale I, at various water saturations. Different saturations of the core plugs (from ∼10 per cent to ∼70 per cent) were obtained by exposing the samples to different relative humidities. Young's modulus, E, and Poisson's ratio, ν, at seismic frequencies (1–155 Hz), and P- and S-wave velocities at ultrasonic frequencies, were measured in a stress range 5–20 MPa. Since tested shales are anisotropic, samples of different orientations have been used to determine Thomsen's anisotropy parameters (Thomsen 1986) and all independent parameters of the elastic stiffness tensor. The experimental data are consistent with TI symmetry, thus confirming that both tested shales can be considered as a TI media. After a short description of the experimental setup, the tested shales, the preparation technique, the experimental conditions (Section 2), and the data processing methods (Section 3), we present the experimental results (Section 4). For each shale type and saturation, dispersion at various stresses is shown for: (i) directional Young's moduli; (ii) directional Poisson's ratios; (iii) directional P- and S-wave velocities; (iv) independent elements of the TI stiffness tensors; and (v) Thomsen's anisotropy parameters. Finally, we discuss how the observed different stress sensitivity at seismic and ultrasonic frequencies is linked with a stress dependency of dispersion.

2 MATERIALS AND METHODS

2.1 Sample characterization

Mancos shale, used in this work, is an outcrop shale from the Western United States, considered as an analogue for some shale gas reservoir rocks. It contains thin clayey laminations with fine grained quartz texture and exhibits transverse isotropy. Total Organic Content (TOC) of Mancos shale varies between ∼1 per cent and 1.5 per cent depending on the origin of the shale. Data available in the literature (e.g. Kellogg 1977; Sarker & Batzle 2010; Holt *et al.* 2012; Morsy *et al.* 2013) report porosities of Mancos shale between 1 per cent and 11 per cent. Porosity of the material tested here was not measured directly, however, based on the density measurements of oven-dry samples and mineral composition obtained from the XRD test, it is estimated to be 7 per cent ± 1 per cent. Measurements performed on other samples cut from the same batch yielded a cross-bedding gas permeability of 6–10 nD.

Pierre shale I, used in this work, is an outcrop shale from North Dakota, considered as an analogue for some caprock formations. It is notably softer than Mancos shale and has a higher porosity that varies between 10 per cent and 25 per cent (e.g. Schultz *et al.* 1980; Olgaard *et al.* 1995; Holt *et al.* 2015) depending on the origin of the shale. Pierre shale I core plugs were drilled from two batches of outcrop material preserved in oil prior to the experiment. XRD data shows that samples S07 and S11 (see Table 1) consist of about 48 wt% clays, 44 wt% silicates (27 wt% quartz) and around 6 wt% of carbonates. All remaining core plugs contain about 42 wt% clays, 48 wt% silicates (30 wt% quartz) and around 7 wt% of carbonates. Based on the density measurements of as-received samples, which were nearly fully saturated (strain measurements performed during previous experiments with the samples cut from the same batch of the material as used here shows that, while exposing the core plugs to brine under stress, the strains stabilize within ∼50 hrs), and mineral composition taken from XRD tests,

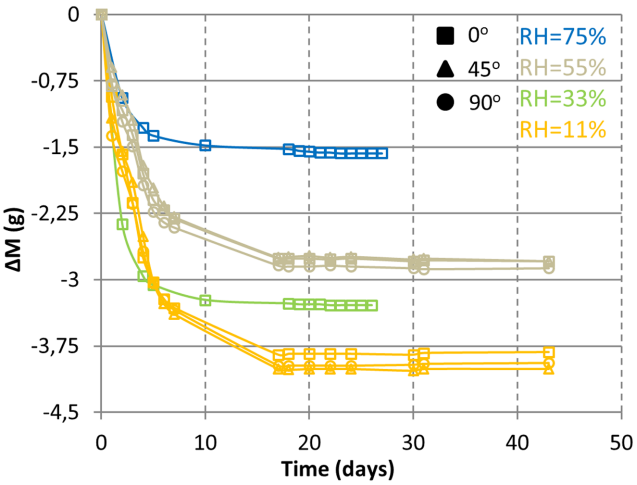

Figure 1. Mass change of Pierre shale I core plugs used during experiments. To change saturations of the core plugs as-received samples were exposed to different relative humidities (RHs) and stabilizing under room temperature.

porosities of our samples are estimated to be 16 per cent ± 1 per cent. Due to internal texture, Pierre shale I exhibits transverse isotropy (e.g. Schultz *et al.* 1980).

2.2 Sample preparation and experimental conditions

2.2.1 Mancos shale

Three differently oriented (0°, 45° and 90° angle with respect to the symmetry axis of shale) cylindrical samples, with a diameter of 1 inch and a length of 2 inches, were cut from a single batch of the outcrop material preserved in oil (see Table 1). To maintain the as-received state of the samples (partial saturation of about 72 per cent—see Section 3.2), core plugs were mounted into the compaction cell and sealed within ∼1 hr after being removed from the preservation oil, upstream and downstream pore pressure valves had been closed, and no additional pore fluid was applied within the pressure vessel. Initially, samples were loaded hydrostatically to 5 MPa. Afterwards, the axial stress (σ_{ax}) was increased by 2 MPa and first low frequency measurement was conducted after the samples had stabilized (strains were constant for at least 30 min). Later, the samples were exposed to incremental isotropic loading, and measurements were performed at every 5 MPa interval, up to a maximum confining stress $P_{\text{conf}} = 20$ MPa ($\sigma_{ax} = 22$ MPa) after the samples were consolidated (the loading speed was 10 MPa h^{-1}). The tests were carried out at room temperature, and the pore pressure was kept at atmospheric level (no pore-pressure control).

2.2.2 Pierre shale

Eight different cylindrical Pierre shale I core plugs, with a diameter of 1 inch and a length of 2 inches, were drilled from outcrop material preserved in oil. Samples were cut with an angle of 0°, 45° and 90° with respect to the symmetry axis of shale (see Table 1). Before conducting the experiments, the saturations of the samples were changed by exposing them to different relative humidities (RHs): As-received samples were stabilized at room temperature in desiccators containing saturated solutions of different salts (Greenspan 1977) shown in Table 1. The RH inside the desiccators was monitored with hygrometers. All samples lost weight (see Fig. 1) and shrank (see Table 1). Mass changes were recorded on a daily basis. Experiments were performed after the weight of the samples did not change by more than 0.01 g over the course of 1 week, which took around 6–7 weeks. The core plugs were mounted into the compaction cell within ∼1 hr after removing them from the desiccators, which most likely preserved their partial saturation. As for Mancos shale, upstream and downstream pore pressure valves were closed, no additional pore fluid was applied within the pressure vessel, and the measurements were performed at room temperature and under atmospheric pore pressure. Also, the stabilization criterion was the same as for Mancos shale. The loading procedure was nearly the same as for Mancos shale, however, the loading speed was two times lower and the stress states were slightly different: (i) $P_{\text{conf}} = 3{,}5$ MPa, $\sigma_{ax} = 5$ MPa; (ii) $P_{\text{conf}} = 8{,}5$ MPa, $\sigma_{ax} = 10$ MPa; (iii) $P_{\text{conf}} = 13{,}5$ MPa, $\sigma_{ax} = 15$ MPa; (iv) $P_{\text{conf}} = 18{,}5$ MPa, $\sigma_{ax} = 20$ MPa. Throughout the paper, we will relate the observed changes in the rock properties to the change of water saturation. Note however, that the exposure to different RH changes not only the water saturation but also other important parameters such as the porosity/volume (see Table 1).

2.3 Experimental setup

The experiments were performed in the Formation Physics laboratory at SINTEF Petroleum Research, within a triaxial compaction cell allowing for measurements of static and dynamic properties of tested specimens within single experiment. The apparatus allows for measuring

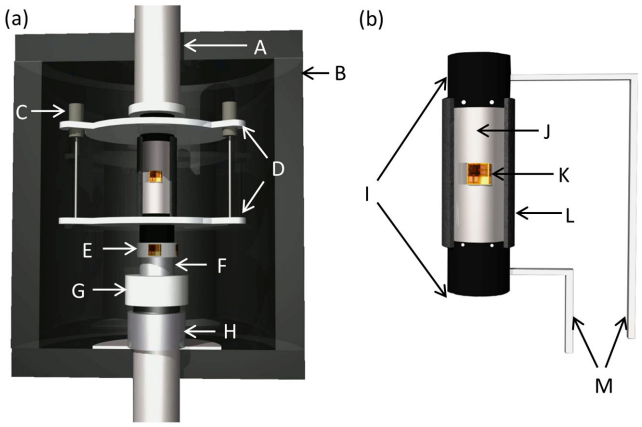

Figure 2. Schematic drawings of the experimental setup (a) and the sample with attached strain gauges (b). Indicated on the drawings are: piston (A), pressure vessel (B), linear variable displacement transducer (LVDT) (C), adapter plates holding LVDT's (D), aluminium standard with attached semiconductor strain gauges (E), piezoelectric force sensor (F), piezoelectric actuator (G), internal load cell (H), top and bottom endcaps with embedded compressional and shear wave transducers and pore-fluid lines (I), sample (J), strain gauges attached to sample (K), rubber sleeve around the sample that seals the sample from the confining stress oil (L), and pore-fluid lines (M).

static rock deformations, ultrasonic velocities (*P*- and *S*-wave velocities along the sample axis) and dynamic elastic properties (Young's modulus, Poisson's ratio) at seismic frequencies (1–155 Hz), under deviatoric stresses and pore pressures. Ultrasonic properties are determined with the use of pulse transmission technique, while elastic parameters at seismic frequencies are obtained by forced deformation method (e.g. Spencer 1981) with small strains ($<10^{-6}$) measured locally on the sample (by the attached strain gauges). A schematic drawing of the apparatus is shown in Fig. 2.

The sample stack is composed of: (i) a rigid piston; (ii) two rigid end-caps equipped with pore-fluid lines for pore fluid substitution/pore pressure control, and with embedded pair of compressional (*P*) and shear (*S*) wave transducers (central frequency of both transducers—500 kHz) for determination of ultrasonic velocities; (iii) a rock sample placed between the end-caps with strain gauges attached to its surface; (iv) adapter plates holding three linear variable displacement transducers (LVDT's) used during the static phase of the experiment; (v) an aluminium piece with semiconductor strain gauges used for phase shift measurements during low-frequency experiments; (vi) a piezoelectric force sensor used for a direct measurement of the force modulations at seismic frequencies; (vii) a piezoelectric actuator used to generate the displacement modulations at seismic frequencies; (viii) an internal load cell for measuring deviatoric stress changes during static phase of experiment. The entire stack is mounted on the base flange of the pressure vessel, equipped with fluid lines for confining and pore pressure control as well as necessary electric feedthroughs. During the experiments, the compaction cell is placed inside a mechanical loading frame exerting axial force on the sample stack through a rigid piston. A detailed description of the apparatus together with the sample/strain gauge fitting procedure is given in Szewczyk *et al.* (2016).

2.4 Sources and magnitudes of experimental errors

The errors in the ultrasonic velocity measurements associated with possible misalignment of the ultrasonic transducers with respect to the bedding, and picking of the arrivals are estimated to be between 2–5 per cent. Systematic errors in the seismic frequencies measurements associated with: (i) sample bulging, (ii) possible small misalignment of the stack (decreasing with increasing confining pressure), (iii) non-parallel alignment of the strain gauges with respect to the sample axis, (iv) electronic noise, and (v) possible energy dissipation due to friction between the rubber jacket and the confining pressure oil; were quantified by performing seismic-frequency measurements with non-dispersive standard materials (aluminium and PEEK). For the standard materials, the experimental errors for seismic Young's modulus and Poisson's ratio did not exceed 5 per cent. The errors associated with heterogeneities of the samples exhibiting local strain variations on a scale larger than the size of the strain gauges (e.g. internal variations of lamination or drilling related inaccuracies) may introduce additional errors (see data analysis procedure in Section 3). At ultrasonic frequencies, sensitivity studies have shown that, in the case of TI media, a 10° orientation error for a nominally 45°-oriented sample, may lead to an 11 per cent error in determination of vertical Young's modulus and around ± 0.07 error in determination of Poisson's ratio. At seismic frequencies, similar sensitivity studies indicate 8 per cent error in determination of vertical *S*-wave velocity, whereas *P*-wave velocity is not affected by orientation errors of nominally 45°-oriented sample. In addition, since the core plugs were not tested under purely hydrostatic pressure (small additional axial stress applied), a small error associated with different stress states of 0°, 45° and 90° oriented samples is expected.

3 DATA PROCESSING METHODS

3.1 Conversion between engineering parameters and elastic velocities in TI medium

The forced deformation method and the pulse transmission technique used during seismic and ultrasonic measurements, respectively, provide two different sets of dynamic properties. Therefore, in order to compare the obtained results, conversion between those two different moduli is required. Generally, in anisotropic, elastic material stress (σ_{ij}) and strain (ε_{kl}) tensors are linearly related by a stiffness tensor (C_{ijkl})—Hooke's law:

$$\sigma_{ij} = C_{ijkl}\,\varepsilon_{kl}, \tag{1}$$

where Einstein's summation convention applies. For transversely isotropic materials in which the z-axis is the unique symmetry axis, the elastic stiffness tensor can be written as a matrix using Voigt notation (Voigt 1928; Nye 1985):

$$C_{ij} = \begin{bmatrix} C_{11} & C_{12} & C_{13} & 0 & 0 & 0 \\ C_{12} & C_{11} & C_{13} & 0 & 0 & 0 \\ C_{13} & C_{13} & C_{33} & 0 & 0 & 0 \\ 0 & 0 & 0 & C_{44} & 0 & 0 \\ 0 & 0 & 0 & 0 & C_{44} & 0 \\ 0 & 0 & 0 & 0 & 0 & C_{66} \end{bmatrix}, \tag{2}$$

with $C_{12} = C_{11} - 2C_{66}$.

The anisotropy of a TI material can be characterized by three parameters introduced by Thomsen (1986):

$$\varepsilon = \frac{C_{11} - C_{33}}{2C_{33}}, \tag{3}$$

$$\gamma = \frac{C_{66} - C_{44}}{2C_{44}}, \tag{4}$$

$$\delta = \frac{(C_{13} + C_{44})^2 - (C_{33} - C_{44})^2}{2C_{33}\,(C_{33} - C_{44})}. \tag{5}$$

The elastic stiffness matrix contains five independent stiffness parameters, C_{11}, C_{33}, C_{44}, C_{66} and C_{13}, that fully characterize TI materials. Therefore, identifying all independent stiffnesses, C_{ij}'s, and using proper combination of those parameters, allow for conversion between different sets of measured moduli. Determination of all independent stiffness parameters from ultrasonic measurements requires the following properties of the studied material: (i) phase velocities of *P*- and *S*-waves traveling along the symmetry axis (further denoted with subscript V); (ii) phase velocities of *P*- and *S*-waves traveling within the symmetry plane (further denoted with subscript H); (iii) phase velocity of 'quasi *P*-wave' or 'quasi *S*-wave' with the wave vector oriented at an angle θ with respect to the material's symmetry axis (further denoted as $V_{\mathrm{qP}}(\theta)$ or $V_{\mathrm{qS}}(\theta)$); and (iv) material bulk density (ρ). The equations that form a basis for an inversion from the velocities to the independent stiffness parameters are (e.g. Helbig 1994; Mavko *et al.* 2009):

$$V_{\mathrm{PV}} = \sqrt{\frac{C_{33}}{\rho}}, \tag{6}$$

$$V_{\mathrm{SV}} = \sqrt{\frac{C_{44}}{\rho}}, \tag{7}$$

$$V_{\mathrm{PH}} = \sqrt{\frac{C_{11}}{\rho}}, \tag{8}$$

$$V_{\mathrm{SH}} = \sqrt{\frac{C_{66}}{\rho}}, \tag{9}$$

$$V_{\mathrm{qP}}(\theta) = \sqrt{\frac{C_{11}\sin^2\theta + C_{33}\cos^2\theta + C_{44} + \sqrt{\left[(C_{11} - C_{44})\sin^2\theta - (C_{33} - C_{44})\cos^2\theta\right]^2 + 4[C_{13} + C_{44}]^2\sin^2\theta\cos^2\theta}}{2\rho}}, \tag{10}$$

$$V_{\mathrm{qS}}(\theta) = \sqrt{\frac{C_{11}\sin^2\theta + C_{33}\cos^2\theta + C_{44} - \sqrt{\left[(C_{11} - C_{44})\sin^2\theta - (C_{33} - C_{44})\cos^2\theta\right]^2 + 4[C_{13} + C_{44}]^2\sin^2\theta\cos^2\theta}}{2\rho}}. \tag{11}$$

In laboratory measurements at seismic frequencies within a conventional compaction cell (where only axial stress and confining pressure can be controlled), Young's moduli and Poisson's ratios are recorded for stress excitations in the axial direction. Here, the determination

of the five independent stiffness parameters requires measurements with three differently oriented samples (0° and 90° with respect to the symmetry axis, and an additional oblique angle). After measuring the directional Young's moduli and Poisson's ratios, the independent stiffness parameters can be inverted from (e.g. Helbig 1994; Mavko *et al.* 2009):

$$E_{\mathrm{V}} = C_{33} - \frac{C_{13}^2}{C_{11} - C_{66}}, \tag{12}$$

$$\nu_{\mathrm{VH}} = \frac{C_{13}}{2(C_{11} - C_{66})}, \tag{13}$$

$$\mathrm{E_H} = \frac{4C_{66}\left[(C_{11} - C_{66})\,C_{33} - C_{13}^2\right]}{C_{11}C_{33} - C_{13}^2}, \tag{14}$$

$$\nu_{\mathrm{HV}} = \frac{2C_{66}C_{13}}{C_{11}C_{33} - C_{13}^2}, \tag{15}$$

$$\nu_{\mathrm{HH}} = \frac{(C_{11} - 2C_{66})C_{33} - C_{13}^2}{C_{11}C_{33} - C_{13}^2}, \tag{16}$$

$$\frac{1}{E\,(\theta)} = \frac{\cos^4\theta}{E_{\mathrm{V}}} + \frac{\sin^4\theta}{E_{\mathrm{H}}} + \frac{\sin^2\theta\cos^2\theta\,[(C_{11} - C_{66})\,C_{33} - (C_{13} + C_{44})\,C_{13}]}{C_{44}\left[(C_{11} - C_{66})\,C_{33} - C_{13}^2\right]}. \tag{17}$$

Determination of all independent stiffness parameters at each investigated frequency allows to reuse eqs (6)–(17) for conversion between elastic velocities and engineering parameters.

In the case of Pierre shale (samples exposed to RH = 33 per cent and RH = 75 per cent), only core plugs oriented at 0° with respect to symmetry axis were available for testing. Thus, the procedure described above could not be applied. In order to derive the elastic stiffness parameters of those specimens we have assumed a linear dependence of Thomsen's parameters on RH to which the samples were exposed. After experimentally determining Thomsen's parameters for samples stabilized at RH = 19 per cent and RH = 55 per cent, for each of the presented frequencies we have independently extrapolated ε, γ and δ to other RH values and determined the elastic stiffness parameters at seismic frequencies by inverting eqs (3)–(6) and (12) and (13) (at ultrasonic frequencies by inverting eqs 3–6 and 6 and 7), which leads to two independent solutions. The choice of the physically valid solution was dictated by the following inequalities that are a consequence of positive elastic energy requirement (the elasticity matrix is positive definite)for TI media (e.g. Nye 1985):

$$C_{44} > 0; \quad C_{66} > 0; \quad C_{33} > 0; \quad C_{11} > C_{66} > 0; \quad (C_{11} - C_{66})\,C_{33} - C_{13}^2 > 0. \tag{18}$$

3.2 Determination of saturation levels

3.2.1 Mancos shale

Determination of saturation of as-received Mancos shale was based on the mineral density, XRD composition and measured bulk density of the oven dried (105 °C) specimen cut from the same batch as samples tested here. XRD data and mineral densities were used to calculate the expected density in the fictitious case of zero porosity. From those calculations and the measured bulk density of the oven-dried core plug, the porosity could be determined. Here, we have assumed that the oven dried sample has a remaining water saturation of 2 per cent (Chenevert & Amanullah 1997 has shown that clay containing rocks cannot be completely dehydrated by exposing them to 105 °C). Finally, the saturation was calculated as a ratio of the volume of the water corresponding to the loss of mass during drying, and total available pore volume determined with the use of previously calculated porosity and the volume changes measured during drying. The saturation of as-received Mancos shale was estimated in this way to be 72 ± 5 per cent.

3.2.2 Pierre shale

Conceptually, determination of the saturation of Pierre shale core plugs was nearly similar to the procedure described for Mancos shale. Again, based on the XRD data and mineral densities, the expected density in the fictitious case of zero porosity was calculated. This time however, this fictitious density was compared with the measured density of as-received samples (known to be nearly fully saturated), and the porosity was calculated under the assumption that as-received samples had a water saturation of 98 per cent. We have assumed that the obtained porosity is representative for all samples, and the RH-to-saturation conversion was done by comparing the total pore volume with the volume of water corresponding to the loss of mass measured during exposure of the samples to different RH (Fig. 1). Again, relative volume changes (assumed to the equal to the pore-volume changes) of the samples during conditioning in the desiccators (see Table 1) were taken into account. Water saturations obtained in this way are listed in Table 1.

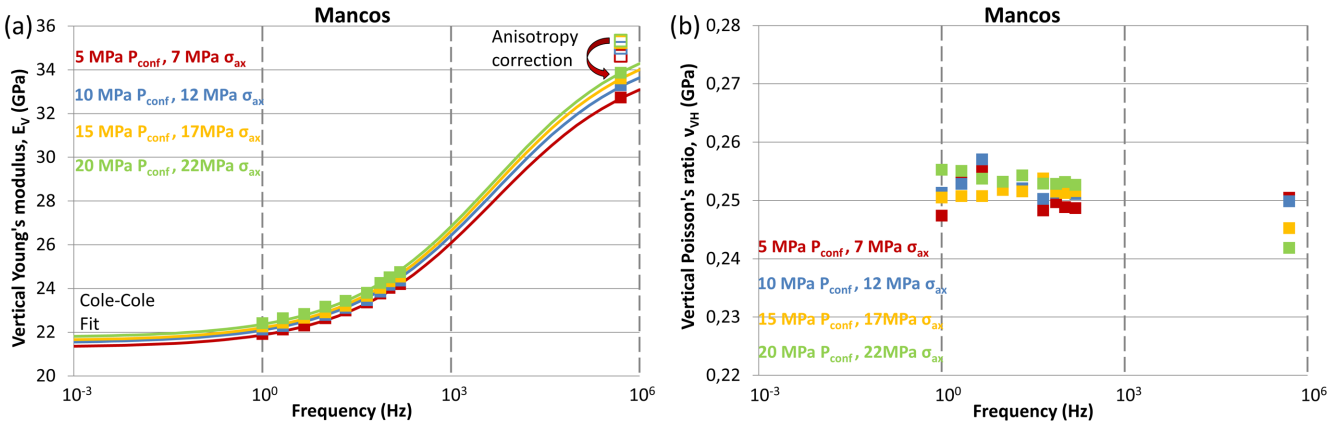

Figure 3. Stress sensitivity of vertical Young's modulus (a) and vertical Poisson's ratio (b) of as-received Mancos shale as a function of frequency. Samples were investigated at room temperature, during isotropic loading with atmospheric pore pressure. Seismic points were measured directly, while ultrasonic filled symbols were determined from measured directional *P*- and *S*-wave velocities. Open symbols at ultrasonic frequencies show the isotropic conversion from V_{PV}, and V_{SP} to E_V and were added to illustrate errors associated with neglecting material anisotropy (anisotropy correction). Solid lines in (a) show manual Cole–Cole fits to the experimental data (Cole & Cole 1941).

3.3 Cole–Cole model of seismic dispersion

Assuming that the Cole–Cole model may be applied for anisotropic rocks (the anelasticity satisfies the Kramers–Kronig integral relations, the system is linear, the attenuation can be described by a single mechanism) and following previous work on attenuation in viscoelastic media (e.g. Spencer 1981; Batzle *et al.* 2006) the Cole–Cole model was used to provide the qualitative manual fit of the measured seismic-dispersion data (Cole & Cole 1941):

$$E' = E_\infty + \frac{E_0 - E_\infty}{2}\left[1 - \frac{\sinh(1-\alpha)\ln\omega\tau_0}{\cosh(1-\alpha)\ln\omega\tau_0 + \cos\frac{\alpha\pi}{2}}\right], \tag{19}$$

$$E'' = \frac{\frac{E_0 - E_\infty}{2}\cos\frac{\alpha\pi}{2}}{\cosh(1-\alpha)\ln\omega\tau_0 + \sin\frac{\alpha\pi}{2}}, \tag{20}$$

here E_∞, E_0 are high- and low-frequency limits of E, $\tau_0$is the relaxation time, E' and E'' stands for real and imaginary part of complex modulus, ω is angular frequency and α is a parameter accounting for the width of the relaxation-time distribution.

4 EXPERIMENTAL RESULTS

4.1 Vertical Young's modulus and Poisson's ratio

Figs 3 and 4 show seismic and ultrasonic stress sensitivity of vertical Young's moduli, E_V, and vertical Poisson's ratios, ν_{VH}, of Mancos shale and Pierre shale, respectively. Filled symbols at ultrasonic frequencies were determined from *P*- and *S*-wave velocity measurements. Open symbols at ultrasonic frequencies represent the isotropic conversion from vertical *P*- and *S*-wave velocities to vertical Young's moduli and were added to illustrate errors associated with neglecting material anisotropy. Solid lines correspond to the manual Cole–Cole fits of data with E_∞ and E_0 being equal to values measured at ultrasonic and 1 Hz frequencies, respectively, whereas α and τ_0 were used as a free parameters (for Mancos shale best fits were obtained for $\alpha = 0.65$ and $\tau_0 \sim 10^{-5}$, whereas for Pierre shale best fits were obtained for $\alpha = 0.65$ and τ_0 was changing between 10^{-2} and 10^{-5} depending on the saturation). The numerical values of seismic (1 Hz) and ultrasonic measurements are summarized in Table 2.

4.1.1 Mancos shale

Strong, nearly stress insensitive, seismic dispersion of ∼50 per cent between seismic and ultrasonic frequencies is observed for E_V (see Table 2). Between 1 and 155 Hz the observed dispersion is ∼10 per cent regardless of the applied stress. Poisson's ratio, ν_{VH}, does not exhibit a significant frequency dependency. The stress sensitivity of Young's modulus, $\frac{\Delta E}{E\Delta\sigma}$, is rather small ($\frac{\Delta E_{V-1\,Hz}}{E_{V-1\,Hz}\Delta\sigma} = 0.15$ per cent MPa^{-1}, $\frac{\Delta E_{V-ultrasonic}}{E_{V-ultrasonic}\Delta\sigma} = 0.23$ per cent MPa^{-1}) at both seismic and ultrasonic frequencies (see Table 2). Seismic and ultrasonic Poisson's ratios seem to increase with stress, however, data points are within experimental errors.

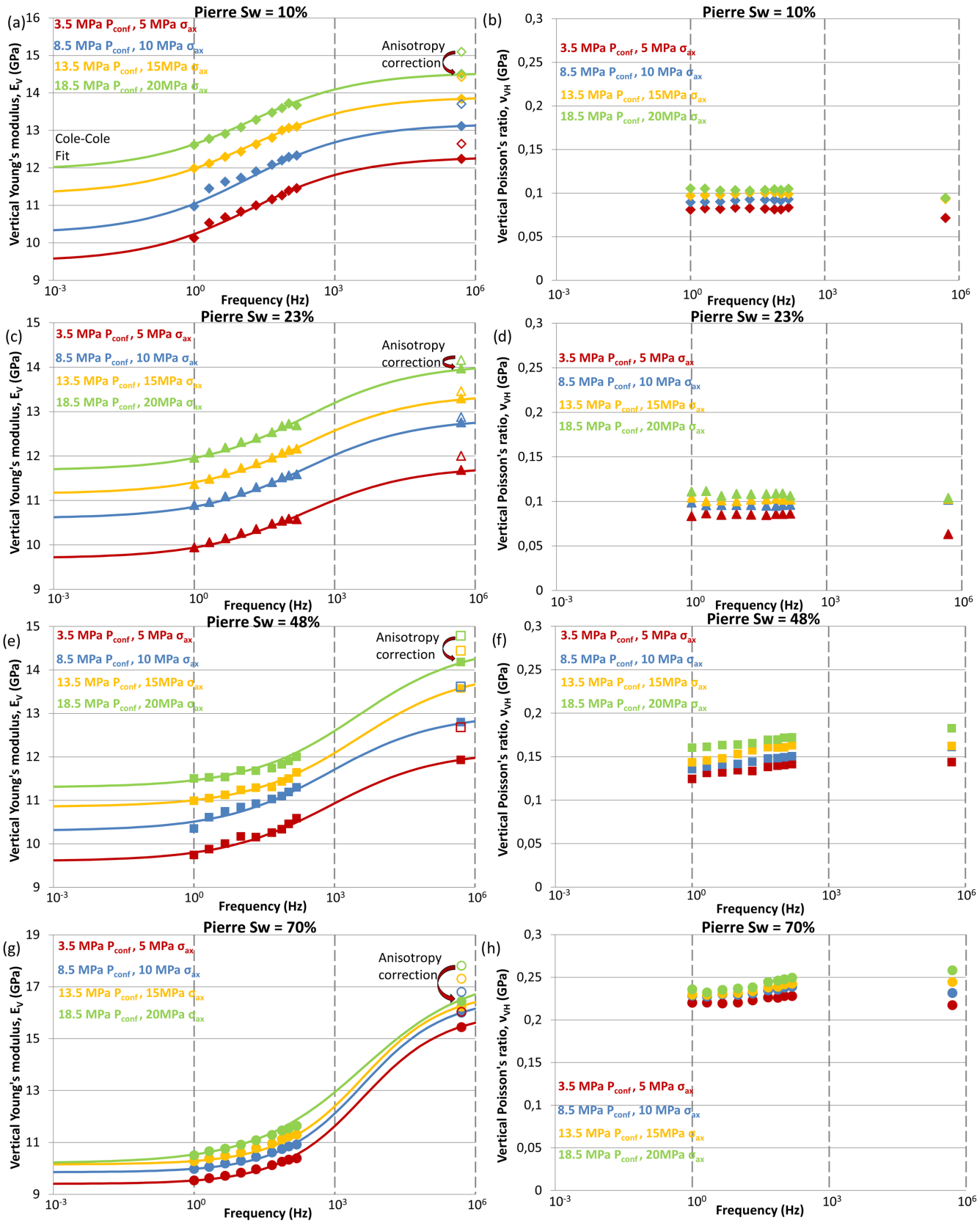

Figure 4. Stress sensitivity of vertical Young's moduli and vertical Poisson's ratios of partially saturated Pierre shale as a function of frequency. Seismic points were measured directly, while ultrasonic filled symbols were determined from measured directional *P*- and *S*-wave velocities. Open symbols at ultrasonic frequencies show the isotropic conversion from V_{PV}, and V_{SP} to E_V and were added to illustrate errors associated with neglecting material anisotropy (anisotropy correction). Samples were investigated at room temperature, during isotropic loading with atmospheric pore pressure. Solid lines show manual Cole–Cole fits to the experimental data (Cole & Cole 1941).

Table 2. List of the vertical Young's moduli together with their stress-sensitivity and the dispersion amplitude, as well as vertical Poisson's ratios obtained during isotropic loading of Mancos shale and differently saturated Pierre shale I samples.

		5 MPa P_{conf}, 7 MPa σ_{ax} (Mancos) 3,5 MPa P_{conf}, 5 MPa σ_{ax} (Pierre)		10 MPa P_{conf}, 12 MPa σ_{ax} (Mancos) 8,5 MPa P_{conf}, 10 MPa σ_{ax} (Pierre)		15 MPa P_{conf}, 17 MPa σ_{ax} (Mancos) 13,5 MPa P_{conf}, 15 MPa σ_{ax} (Pierre)		20 MPa P_{conf}, 22 MPa σ_{ax} (Mancos) 18,5 MPa P_{conf}, 20 MPa σ_{ax} (Pierre)	
		1 Hz	Ultrasonic	1 Hz	Ultrasonic	1 Hz	Ultrasonic	1 Hz	Ultrasonic
Mancos shale	E_V (GPa)	21,91	32,73	22,13	33,31	22,27	33,63	22,41	33,86
	$\frac{\Delta E_V \cdot 100}{E_{V-1\,Hz}}$ (per cent)	49,4		50,52		51,01		51,09	
	$\frac{\Delta E_V \cdot 100}{E_V \Delta\sigma}$ (per cent MPa^{-1})	–	–	–	–	–	–	0,15	0,23
	ν_{VH} (−)	0,247	0,250	0,251	0,249	0,251	0,245	0,255	0,242
Pierre shale $S_w \approx 10$ per cent	E_V (GPa)	10,13	12,24	10,98	13,12	11,99	13,84	12,61	14,51
	$\frac{\Delta E_V \cdot 100}{E_{V-1\,Hz}}$ (per cent)	20,8		19,5		15,4		15,1	
	$\frac{\Delta E_V \cdot 100}{E_V \Delta\sigma}$ (per cent MPa^{-1})	–	–	–	–	–	–	1,63	1,24
	ν_{VH} (−)	0,081	0,072	0,090	0,094	0,097	0,093	0,105	0,095
Pierre shale $S_w \approx 23$ per cent	E_V (GPa)	9,95	11,69	10,90	12,76	11,37	13,30	11,96	13,97
	$\frac{\Delta E_V \cdot 100}{E_{V-1\,Hz}}$ (per cent)	17,5		17,1		17,0		16,8	
	$\frac{\Delta E_V \cdot 100}{E_V \Delta\sigma}$ (per cent MPa^{-1})	–	–	–	–	–	–	1,35	1,3
	ν_{VH} (−)	0,084	0,063	0,099	0,102	0,104	0,103	0,111	0,103
Pierre shale $S_w \approx 48$ per cent	E_V (GPa)	9,74	11,93	10,35	12,80	10,99	13,57	11,51	14,18
	$\frac{\Delta E_V \cdot 100}{E_{V-1\,Hz}}$ (per cent)	22,5		23,7		23,5		23,2	
	$\frac{\Delta E_V \cdot 100}{E_V \Delta\sigma}$ (per cent MPa^{-1})	–	–	–	–	–	–	1,21	1,26
	ν_{VH} (−)	0,124	0,144	0,136	0,161	0,144	0,162	0,160	0,183
Pierre shale $S_w \approx 70$ per cent	E_V (GPa)	9,54	15,45	9,98	16,00	10,28	16,23	10,50	16,44
	$\frac{\Delta E_V \cdot 100}{E_{V-1\,Hz}}$ (per cent)	62,0		60,3		57,9		56,6	
	$\frac{\Delta E_V \cdot 100}{E_V \Delta\sigma}$ (per cent MPa^{-1})	–	–	–	–	–	–	0,67	0,42
	ν_{VH} (−)	0,220	0,217	0,228	0,232	0,230	0,245	0,236	0,258

4.1.2 Pierre shale

Pierre shale exhibits significantly higher stress sensitivity of vertical Young's moduli, E_v. The absolute changes of E_v with stress are nearly similar at seismic and ultrasonic frequencies. However, due to large dispersion, the relative Young's modulus changes are smaller at ultrasonic frequencies. An increase in water saturation causes a decrease of the stress sensitivity. At seismic frequencies (1 Hz) the stress sensitivity of the vertical Young's modulus, $\frac{\Delta E}{E\Delta\sigma}$, decreases by a factor of ~2.5 when increasing saturation from 10 per cent to 70 per cent, while at ultrasonic frequencies the stress sensitivity decreases by a factor of 3 (see Table 2). Note that the increased saturation results in a strong increase of E_v dispersion. At seismic frequencies, the rock softens (reduced Young's modulus and increased Poisson's ratio) with increasing water saturation, while at ultrasonic frequencies, the stiffness dependence on water saturation is more complex since it is also affected by the saturation-dependent dispersion. Unlike for Mancos shale, for Pierre shale, a clear stress sensitivity of vertical Poisson's ratio, ν_{VH}, is observed. Poisson's ratio strongly increases with increasing saturation (see Table 2). Note that the increased saturation also causes slight increase of the Poisson's ratio dispersion. A detailed discussion of the saturation dependence of elastic properties of both Mancos shale and Pierre shale is given in Szewczyk *et al.* (2018).

4.2 Stiffness and velocity anisotropy

The measurement of axial *P*- and *S*-wave velocities as well as Young's moduli and Poisson's ratios for three differently oriented samples allows for a full characterization of stiffness and velocity anisotropy. Fig. 5 shows directional Young's moduli and Poisson's ratios, stiffness parameters, C_{ij}'s, and Thomsen's parameters as a function of frequency for Mancos shale. Figs 6 and 7 show similar set of data obtained for Pierre shale samples ($S_w = 10$ per cent and $S_w = 48$ per cent). Finally, Fig. 8 shows the five independent stiffness parameters, C_{11}, C_{33}, C_{44}, C_{66} and C_{13}, obtained from measurements with only 0°-oriented Pierre shale samples ($S_w = 23$ per cent and $S_w = 70$ per cent), by using extrapolated Thomsen parameters. The numerical values of seismic (1 Hz) and ultrasonic measurements are summarized in Tables 3 and 4.

4.2.1 Mancos shale

For each of the examined stresses, we observe rather large dispersion of all directional seismic Young's moduli and nearly no dispersion of all directional seismic Poisson's ratios. The figures show features characteristic for TI media: (i) the vertical Young's modulus, E_V, is significantly smaller than the one for loading parallel to the bedding, E_H; (ii) Young's modulus for loading under an angle of 45° with respect to bedding is in between E_V and E_H; (iii) Poisson's ratio obtained with the 0°-sample, ν_{VH}, is in between the two Poisson's ratios obtained with the 90°-sample, ν_{HH} and ν_{HV}. The symmetry of TI media requires:

$$\frac{\nu_{VH}}{E_V} = \frac{\nu_{HV}}{E_H}\,. \tag{21}$$

Within the experimental errors, eq. (21) is confirmed by our measurements (see Fig. 5f), which confirms that Mancos shale can be described by TI symmetry. Moreover, the fact that eq. (21) is fulfilled for all frequencies, with Young's moduli exhibiting relatively strong dispersion, gives confidence in the experimental method. Note that the stress sensitivity of Young's moduli exhibits directional dependency. Samples loaded perpendicular to the bedding exhibit a smaller stress sensitivity than samples loaded parallel to the bedding ($\frac{\Delta E_{V-1\,Hz}}{E_{V-1\,Hz}\Delta\sigma} = 0.15$ per cent MPa^{-1}, $\frac{\Delta E_{V-ultrasonic}}{E_{V-ultrasonic}\Delta\sigma} = 0.23$ per cent MPa^{-1}, $\frac{\Delta E_{H-1\,Hz}}{E_{H-1\,Hz}\Delta\sigma} = 0.78$ per cent MPa^{-1}, $\frac{\Delta E_{H-ultrasonic}}{E_{H-ultrasonic}\Delta\sigma} = 0.46$ per cent MPa^{-1}).

For the five independent stiffness parameters the highest seismic dispersion ($\frac{\Delta C_{ij}\cdot 100}{C_{ij-1\,Hz}}$ per cent) is observed for C_{11} (>50 per cent, although comparable with C_{33}) and smallest for C_{44} and C_{66} (~30 per cent). All C_{ij}'s are to a varying degree stress sensitive however, the stress sensitivity is directionally dependant. The highest relative stress sensitivity ($\frac{\Delta C_{ij}\cdot 100}{C_{ij}\Delta\sigma}$ per cent) is observed for C_{11} (although it is comparable with C_{33}) while the lowest for C_{44}.

None of the Thomsen parameters exhibits any significant dispersion between seismic and ultrasonic frequencies. The value of γ, and δ slightly decreases with increasing frequencies however, this drop may be artificial. γ does not show any notable stress sensitivity, indicating that for Mancos shale *S*-wave anisotropy is mostly due to the lithology, and stress induced anisotropy is negligible. Different stress sensitivities of C_{11} and C_{33} results in an increasing value of ε with applied stress (~4 per cent MPa^{-1}). δ increases with stress at seismic frequencies, and is nearly constant during ultrasonic measurements. However, taking into account that δ was determined based on the measurements performed with 45^O-oriented samples, we cannot exclude a relatively large errors (e.g. Sarout *et al.* 2014b).

4.2.2 Pierre shale

The measurements show that Pierre shale at seismic frequencies is softer and less dispersive then Mancos shale. An increase of water content causes a decrease of all directional Young's moduli and a strong increase of all directional Poisson's ratios. Poisson's ratios obtained with low saturated samples are nearly frequency independent, however, an increased water saturation causes an increase in dispersion. At both saturations, all the features characteristic for TI media, as discussed for Mancos shale, are observed for Pierre shale as well. Also the TI-symmetry requirement, eq. (21), is again confirmed by our measurements for all frequencies (see Fig 6f and 7f), which means that Pierre

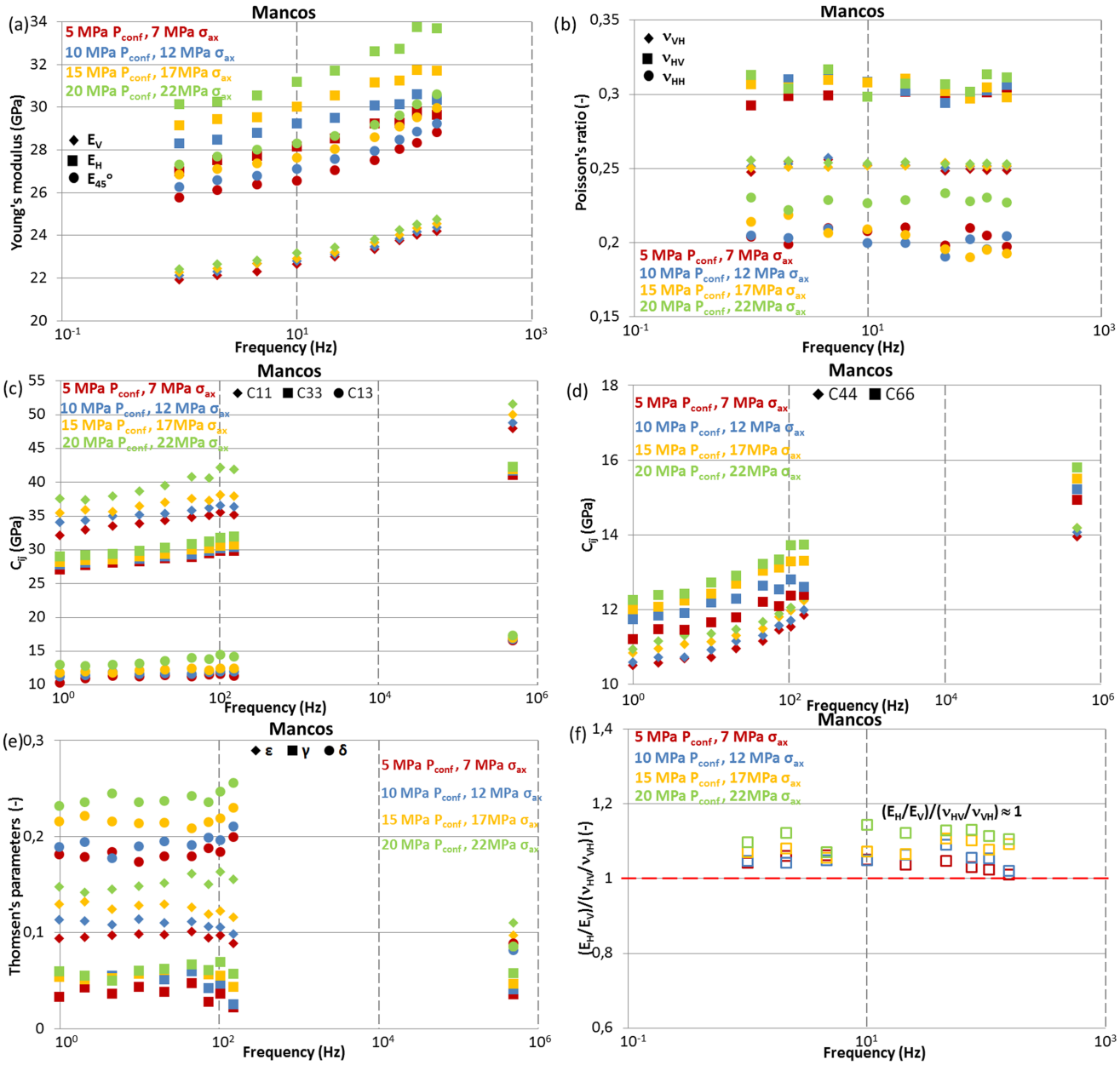

Figure 5. Anisotropic attributes measured with three differently oriented as-received Mancos shale core plugs at different stresses. (a,b) Directional Young's moduli and Poisson's ratios measured at seismic frequencies, (c,d) independent stiffness parameters, C_{ij}'s, determined at seismic and ultrasonic frequencies, (e) Thomsen's parameters, (f) measured $(E_H/E_V)/(\nu_{HV}/\nu_{VH})$, that for perfect TI material should be equal to 1.

shale is consistent with transverse isotropy. In contrast to Mancos shale, for Pierre shale samples with low water content, $\frac{\Delta E}{E\Delta\sigma}$ is about 3 times larger for samples loaded perpendicular to the bedding than for samples loaded parallel to bedding. With increasing water saturation, the stress sensitivity decreases in both directions; however, the effect is stronger for samples loaded perpendicular to the bedding (compare Tables 2 and 4).

For the saturations for which three differently oriented samples were available for testing ($S_w = 10$ per cent and $S_w = 48$ per cent) the qualitative behaviour of the stiffness parameters, C_{ij}'s, is similar to this obtained with Mancos shale. Softening of the sample with increasing water saturation leads to a decrease of all five independent C_{ij}'s. Dispersion is largest for C_{33} and smallest for C_{44}. An increase in saturation results in increased dispersion for all C_{ij}'s. For the remaining saturations, again seismic dispersion is observed for all independent stiffness parameters. Increased water content causes an increase of the dispersion and decrease of the stress sensitivity. Lowest dispersion is observed for C_{13} while highest dispersion is found for C_{11} (see Section 5). Dispersion dependency on saturation is most pronounced for C_{44}.

Figs 6 and 7(g) show the Thomsen's parameters. In the case of low saturation ε and δ clearly decrease with increasing frequency and exhibit strong sensitivity to applied stress (especially at seismic frequencies). Note that the stress increase seem to reduce ε and seem to

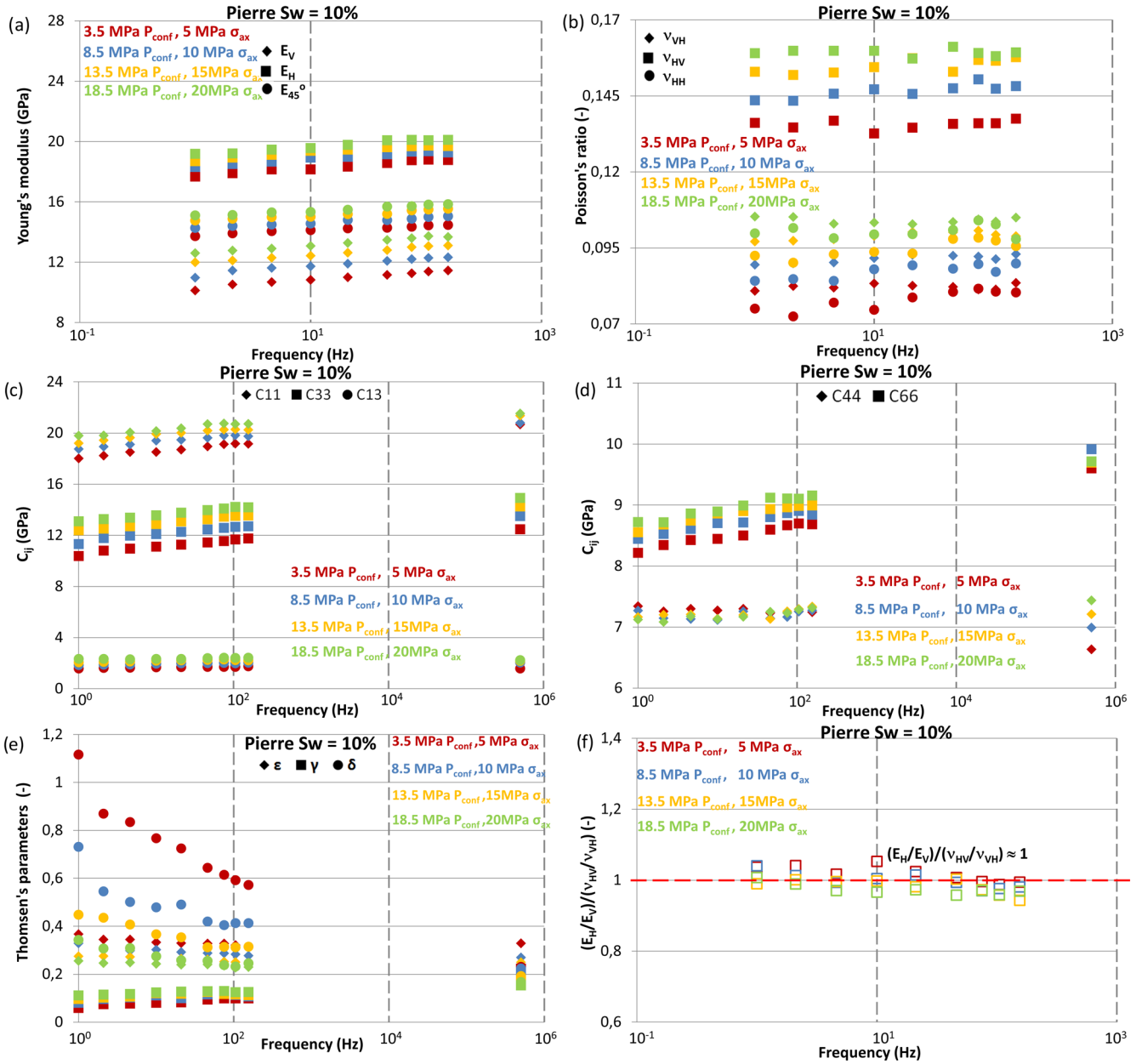

Figure 6. Anisotropic attributes measured with the three differently oriented Pierre shale I core plugs exposed to the RH = 19 per cent at different stresses. (a,b) Directional Young's moduli and Poisson's ratios measured at seismic frequencies, (c,d) independent stiffness parameters, C_{ij}'s, determined at seismic and ultrasonic frequencies, (e) Thomsen's parameters, (f) measured $(E_H/E_V)/(\nu_{HV}/\nu_{VH})$, that for perfect TI material should be equal to 1.

increase γ, which would indicate different stress sensitivities of *P*-wave and *S*-wave anisotropies. The value of δ decreases strongly with applied stress. An increase of the saturation causes all Thomsen parameters to decrease. Mostly affected seems to be δ at seismic frequencies. In addition to a strong reduction of δ, the dispersion of δ is strongly reduced. The stress sensitivity of ε is not strongly affected by the change of the water content, however, γ exhibits a higher sensitivity. Again, a different stress sensitivity is observed at seismic and ultrasonic frequencies (see Tables 3–6).

4.3 Stress sensitivity of velocities

Figs 9 and 10 show dispersion and stress sensitivity of the vertical and horizontal *P*- and *S*-wave velocities of Mancos shale and Pierre shale, respectively. Ultrasonic points were measured directly while velocities at seismic frequencies were calculated from measured vertical Young's modulus and Poisson's ratio. The numerical values of seismic (1 Hz) and ultrasonic measurements are summarized in Tables 5 and 6.

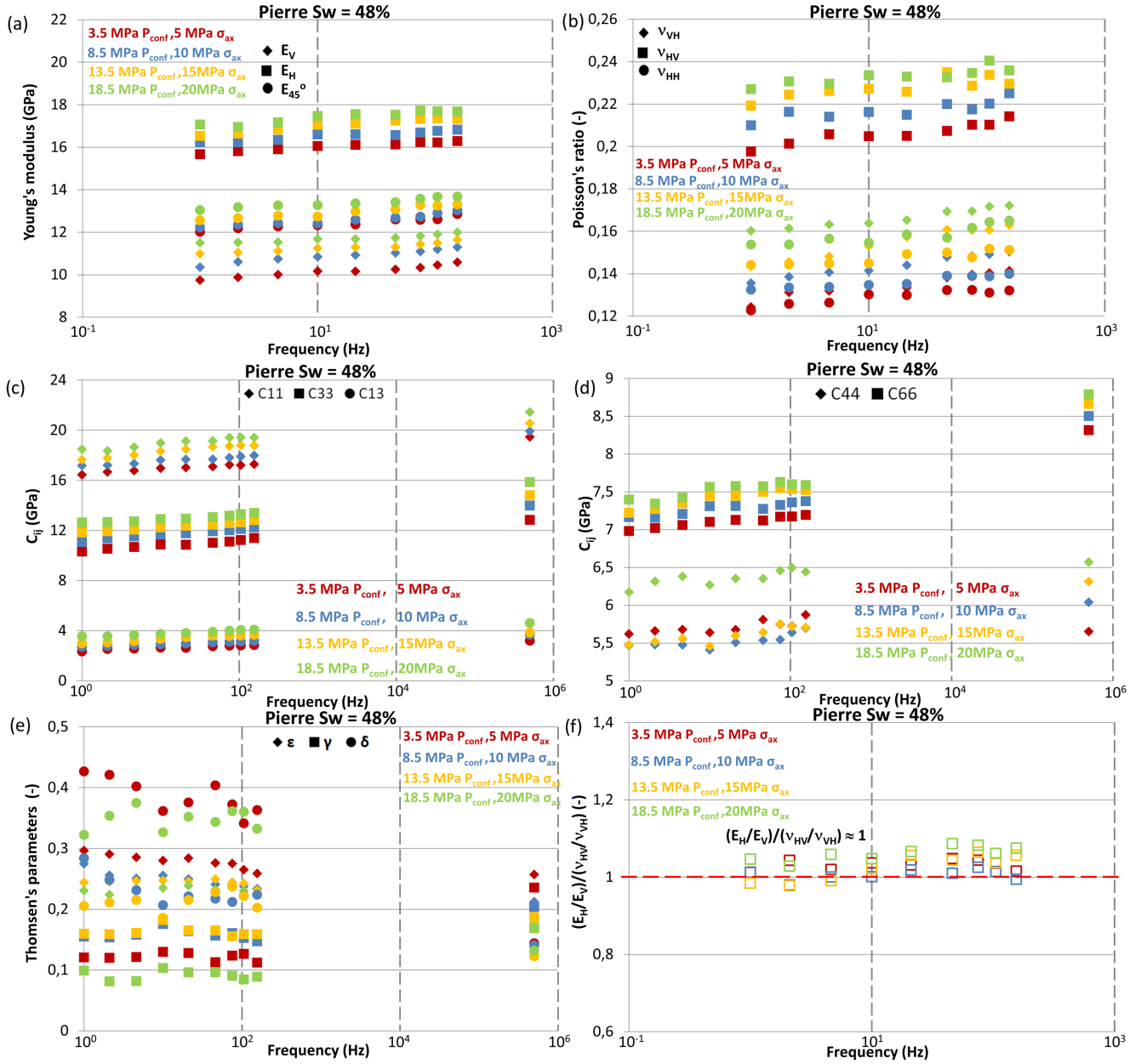

Figure 7. Anisotropic attributes measured with the three differently oriented Pierre shale I core plugs exposed to the RH = 55 per cent at different stresses. (a,b) Directional Young's moduli and Poisson's ratios measured at seismic frequencies, (c,d) independent stiffness parameters, C_{ij}'s, determined at seismic and ultrasonic frequencies, (e) Thomsen's parameters, (f) measured $(E_H/E_V)/(\nu_{HV}/\nu_{VH})$, that for perfect TI material should be equal to 1.

4.3.1 Mancos shale

Large seismic dispersion is observed for both *P*- and *S*-wave velocities. Dispersion of *P*-wave velocities is as high as 23 per cent, and that of *S*-wave velocities as high as 16 per cent. We define stress-sensitivity and strain-sensitivity factors by:

$$S_P = \frac{\Delta V_P}{V_P \Delta \sigma}, \tag{22}$$

$$R_P = \frac{\Delta V_P}{V_P \Delta \varepsilon}. \tag{23}$$

The stress sensitivity factor is frequency dependant (about two times larger at seismic frequencies than at ultrasonic frequencies), and direction dependent (about two times larger for horizontal waves). In accord with the frequency dependent stress sensitivity, dispersion decreases with increasing stress. Also the strain-sensitivity factor exhibits a frequency dependency (about three times larger at seismic frequencies), and a directional dependency (about 4 times larger for horizontal *P*-waves).

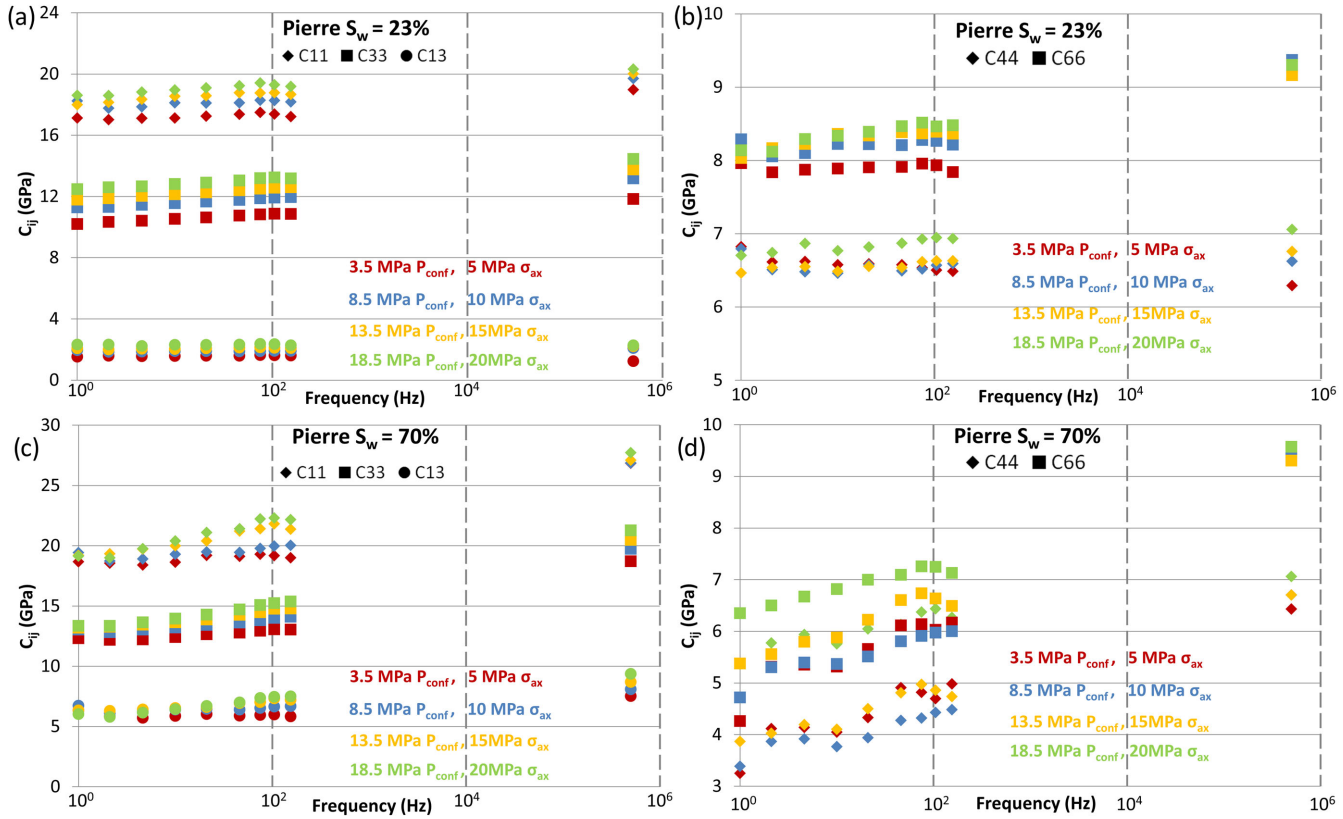

Figure 8. Independent stiffness parameters, C_{ij}'s, determined at seismic and ultrasonic frequencies for Pierre shale I samples ($S_w = 23$ per cent and $S_w = 70$ per cent). Presented data were calculated from Young's moduli and Poisson's ratios (seismic frequencies), and *P*- and *S*-wave velocities (ultrasonic frequencies) measured with 0°-oriented samples by assuming extrapolated Thomsen's parameters.

Table 3. List of the remaining directional Young's moduli, and Poisson's ratios together with the dispersion amplitude and stress-sensitivity, independent stiffness parameters C_{11}, C_{33}, C_{44}, C_{55} and C_{13}, as well as Thomsen's parameters obtained during isotropic loading of Mancos shale.

		5 MPa P_{conf}, 7 MPa σ_{ax}		10 MPa P_{conf}, 12 MPa σ_{ax}		15 MPa P_{conf}, 17 MPa σ_{ax}		20 MPa P_{conf}, 22 MPa σ_{ax}	
		1 Hz	Ultrasonic	1 Hz	Ultrasonic	1 Hz	Ultrasonic	1 Hz	Ultrasonic
Mancos shale	E_H (GPa)	26,98	38,12	28,28	38,82	29,14	39,74	30,12	40,73
	$\frac{\Delta E_H \cdot 100}{E_{H-1\,Hz}}$ (per cent)	41,3		37,3		36,4		35,2	
	$\frac{\Delta E_H \cdot 100}{E_H \Delta\sigma}$ (per cent MPa^{-1})	–	–	–	–	–	–	0,78	0,46
	$E_{45°}$ (GPa)	25,76	35,34	26,26	35,75	26,84	36,09	27,31	36,25
	ν_{HV} (−)	0,293	0,292	0,307	0,291	0,306	0,290	0,313	0,290
	ν_{HH} (−)	0,204	0,277	0,205	0,276	0,214	0,282	0,230	0,288
	C_{11} (GPa)	32,10	47,96	34,05	48,76	35,43	50,02	37,56	51,51
	C_{33} (GPa)	27,03	41,02	27,76	41,67	28,15	41,91	29,01	42,22
	C_{44} (GPa)	10,51	13,95	10,58	14,07	10,84	14,18	10,91	14,16
	C_{66} (GPa)	11,21	14,93	11,74	15,21	12,00	15,50	12,24	15,80
	C_{13} (GPa)	10,34	16,55	11,21	16,76	11,74	16,93	12,93	17,27
	ε (−)	0,094	0,085	0,113	0,085	0,129	0,098	0,147	0,110
	γ (−)	0,033	0,035	0,055	0,041	0,054	0,047	0,060	0,057
	δ (−)	0,181	0,102	0,189	0,082	0,215	0,086	0,232	0,085

4.3.2 Pierre shale

The *P*-wave velocity dispersion in Pierre shale is considerably smaller than in Mancos shale and strongly increases with increasing saturation. As for Mancos shale, we observe that the stress sensitivity varies with frequency, however the effect is smaller. As a result, dispersion decreases with stress. Simultaneously, the average stress-sensitivity factor also depends on the saturation. For relatively dry samples, stress sensitivity is higher at seismic frequencies, while for moist samples it is slightly higher at ultrasonic frequencies (regardless of wave-propagation direction). The strain-sensitivity factor exhibits behaviour similar to the one shown by the stress-sensitivity factor. The dispersion of *S*-wave velocities is smaller compared to the *P*-wave, however the effects of stress and saturation changes remain qualitatively the same as for *P*-wave velocities.

Table 4. List of the remaining directional Young's moduli, and Poisson's ratios together with the dispersion amplitude and stress-sensitivity, independent stiffness parameters C_{11}, C_{33}, C_{44}, C_{55} and C_{13}, as well as Thomsen's parameters obtained during isotropic loading of differently saturated Pierre shale I.

		3,5 MPa P_{conf}, 5 MPa σ_{ax}		8,5 MPa P_{conf}, 10 MPa σ_{ax}		13,5 MPa P_{conf}, 15 MPa σ_{ax}		18,5 MPa P_{conf}, 20 MPa σ_{ax}	
		1 Hz	Ultrasonic	1 Hz	Ultrasonic	1 Hz	Ultrasonic	1 Hz	Ultrasonic
Pierre shale $S_w \approx$ 10 per cent	E_H (GPa)	17,67	20,39	18,32	20,47	18,69	20,90	19,18	21,05
	$\frac{\Delta E_H \cdot 100}{E_{H-1\,Hz}}$ (per cent)	15,4		11,7		11,8		9,8	
	$\frac{\Delta E_H \cdot 100}{E_H \Delta\sigma}$ (per cent MPa^{-1})	–	–	–	–	–	–	0,57	0,22
	E_{45° (GPa)	13,73	14,24	14,27	15,20	14,76	15,77	15,11	16,32
	ν_{HV} (−)	0,136	0,119	0,144	0,147	0,153	0,141	0,159	0,137
	ν_{HH} (−)	0,075	0,062	0,084	0,032	0,092	0,078	0,100	0,083
	C_{11} (GPa)	18,01	20,67	18,75	20,80	19,20	21,36	19,79	21,53
	C_{33} (GPa)	10,38	12,47	11,31	13,50	12,39	14,25	13,10	14,93
	C_{44} (GPa)	7,34	6,64	7,27	6,99	7,17	7,21	7,13	7,44
	C_{66} (GPa)	8,22	9,60	8,45	9,92	8,55	9,70	8,72	9,72
	C_{13} (GPa)	1,58	1,58	1,84	2,05	2,07	2,17	2,33	2,23
	ε (−)	0,367	0,329	0,329	0,270	0,275	0,245	0,255	0,221
	γ (−)	0,060	0,224	0,081	0,209	0,097	0,172	0,112	0,153
	δ (−)	1,116	0,231	0,732	0,224	0,448	0,192	0,343	0,168
Pierre shale $S_w \approx$ 23 per cent	E_H (GPa)	16,85	18,83	17,80	19,36	17,50	19,57	17,98	19,87
	$\frac{\Delta E_H \cdot 100}{E_{H-1\,Hz}}$ (per cent)	11,8		8,8		11,8		10,5	
	$\frac{\Delta E_H \cdot 100}{E_H \Delta\sigma}$ (per cent MPa^{-1})	–	–	–	–	–	–	0,45	0,37
	E_{45° (GPa)	12,45	12,99	13,18	14,15	13,18	14,57	14,83	16,08
	ν_{HV} (−)	0,141	0,102	0,161	0,154	0,160	0,151	0,167	0,148
	ν_{HH} (−)	0,058	0,027	0,074	0,033	0,089	0,068	0,105	0,068
	C_{11} (GPa)	17,13	18,97	18,24	19,72	18,00	20,021	18,61	20,33
	C_{33} (GPa)	10,2	11,84	11,29	13,18	11,80	13,76	12,48	14,45
	C_{44} (GPa)	6,82	6,29	6,78	6,63	6,47	6,76	6,71	7,06
	C_{66} (GPa)	7,96	9,16	8,29	9,37	8,03	9,16	8,14	9,31
	C_{13} (GPa)	1,53	1,24	1,97	2,10	2,08	2,23	2,33	2,29
	ε (−)	0,340	0,301	0,308	0,248	0,263	0,228	0,246	0,204
	γ (−)	0,083	0,228	0,110	0,207	0,121	0,178	0,107	0,159
	δ (−)	0,848	0,197	0,558	0,192	0,354	0,165	0,335	0,154
Pierre shale $S_w \approx$ 48 per cent	E_H (GPa)	15,68	18,44	16,23	18,76	16,53	19,29	17,07	19,79
	$\frac{\Delta E_H \cdot 100}{E_{H-1\,Hz}}$ (per cent)	17,6		15,6		16,7		15,9	
	$\frac{\Delta E_H \cdot 100}{E_H \Delta\sigma}$ (per cent MPa^{-1})	–	–	–	–	–	–	0,59	0,49
	E_{45° (GPa)	12,02	12,74	12,23	13,70	12,56	14,42	13,05	15,15
	ν_{HV} (−)	0,198	0,222	0,210	0,236	0,219	0,231	0,227	0,255
	ν_{HH} (−)	0,123	0,109	0,133	0,103	0,144	0,113	0,154	0,126
	C_{11} (GPa)	16,46	19,46	17,19	19,93	17,64	20,55	18,48	21,46
	C_{33} (GPa)	10,33	12,85	11,09	13,99	11,85	14,82	12,64	15,87
	C_{44} (GPa)	5,62	5,65	5,47	6,04	5,48	6,31	6,17	6,57
	C_{66} (GPa)	6,98	8,32	7,17	8,50	7,23	8,67	7,40	8,79
	C_{13} (GPa)	2,36	3,20	2,72	3,68	2,99	3,86	3,55	4,63
	ε (−)	0,296	0,257	0,275	0,212	0,244	0,193	0,231	0,176
	γ (−)	0,121	0,236	0,155	0,204	0,160	0,186	0,099	0,169
	δ (−)	0,427	0,144	0,284	0,141	0,206	0,123	0,322	0,132
Pierre shale $S_w \approx$ 70 per cent	E_H (GPa)	12,33	22,89	13,30	22,91	14,34	22,98	15,58	23,01
	$\frac{\Delta E_H \cdot 100}{E_{H-1\,Hz}}$ (per cent)	85,7		72,3		60,3		47,7	
	$\frac{\Delta E_H \cdot 100}{E_H \Delta\sigma}$ (per cent MPa^{-1})	–	–	–	–	–	–	1,76	0,04
	E_{45° (GPa)	8,80	16,14	9,23	16,82	10,15	17,00	13,29	18,61
	ν_{HV} (−)	0,285	0,322	0,304	0,327	0,320	0,338	0,350	0,357
	ν_{HH} (−)	0,447	0,198	0,409	0,201	0,334	0,205	0,226	0,188
	C_{11} (GPa)	18,67	26,85	19,44	26,86	19,20	27,10	19,15	27,72
	C_{33} (GPa)	12,33	18,72	13,05	19,75	13,20	20,49	13,35	21,28
	C_{44} (GPa)	3,25	6,44	3,39	6,71	3,87	6,71	5,37	7,06
	C_{66} (GPa)	4,26	9,55	4,72	9,41	5,38	9,31	6,35	9,57
	C_{13} (GPa)	6,34	7,52	6,72	8,09	6,35	8,70	6,03	9,37
	ε (−)	0,257	0,217	0,244	0,180	0,227	0,162	0,217	0,151
	γ (−)	0,155	0,242	0,197	0,201	0,195	0,194	0,092	0,178
	δ (−)	0,043	0,096	0,035	0,095	0,071	0,084	0,311	0,112

Table 5. List of *P*- and *S*-wave velocities together with the dispersion amplitudes obtained during isotropic loading of as-received Mancos shale and differently saturated Pierre shale I core plugs.

		5 MPa P_{conf}, 7 MPa σ_{ax} (Mancos) 3,5 MPa P_{conf}, 5 MPa σ_{ax} (Pierre)		10 MPa P_{conf}, 12 MPa σ_{ax} (Mancos) 8,5 MPa P_{conf}, 10 MPa σ_{ax} (Pierre)		15 MPa P_{conf}, 17 MPa σ_{ax} (Mancos) 13,5 MPa P_{conf}, 15 MPa σ_{ax} (Pierre)		20 MPa P_{conf}, 22 MPa σ_{ax} (Mancos) 18,5 MPa P_{conf}, 20 MPa σ_{ax} (Pierre)	
		1 Hz	Ultrasonic	1 Hz	Ultrasonic	1 Hz	Ultrasonic	1 Hz	Ultrasonic
Mancos shale	V_{PV} (m s^{-1})	3241	3992	3284	4024	3307	4035	3358	4050
		23,2		22,5		22,0		20,6	
	$\frac{\Delta V_{PV} \cdot 100}{V_{PV-1Hz}}$ (per cent)								
	V_{PH} (m s^{-1})	3532	4317	3637	4353	3711	4409	3820	4474
		22,2		19,7		18,8		17,1	
	$\frac{\Delta V_{PH} \cdot 100}{V_{PH-1Hz}}$ (per cent)								
	V_{SV} (m s^{-1})	2021	2328	2028	2337	2052	2347	2062	2346
	V_{SH} (m s^{-1})	2087	2408	2136	2431	2160	2454	2181	2478
Pierre shale $S_w \approx 10$ per cent	V_{PV} (m s^{-1})	2127	2330	2219	2425	2323	2485	2389	2550
		9,5		9,3		7,0		6,7	
	$\frac{\Delta V_{PV} \cdot 100}{V_{PV-1Hz}}$ (per cent)								
	V_{PH} (m s^{-1})	2801	3000	2857	3010	2891	3043	2936	3062
		7,1		5,4		5,3		4,3	
	$\frac{\Delta V_{PH} \cdot 100}{V_{PH-1Hz}}$ (per cent)								
	V_{SV} (m s^{-1})	1788	1700	1780	1745	1767	1768	1762	1800
	V_{SH} (m s^{-1})	1892	2045	1918	2078	1930	2050	1949	2057
Pierre shale $S_w \approx 23$ per cent	V_{PV} (m s^{-1})	2088	2250	2197	2374	2246	2425	2310	2485
		7,8		8,1		8,0		7,6	
	$\frac{\Delta V_{PV} \cdot 100}{V_{PV-1Hz}}$ (per cent)								
	V_{PH} (m s^{-1})	2706	2848	2793	2903	2774	2926	2821	2948
		5,3		3,9		5,5		4,5	
	$\frac{\Delta V_{PH} \cdot 100}{V_{PH-1Hz}}$ (per cent)								
	V_{SV} (m s^{-1})	1708	1640	1704	1683	1662	1700	1693	1737
	V_{SH} (m s^{-1})	1845	1979	1882	2001	1853	1979	1865	1994
Pierre shale $S_w \approx 48$ per cent	V_{PV} (m s^{-1})	2095	2337	2171	2438	2244	2510	2318	2597
		11,6		12,3		11,9		12,0	
	$\frac{\Delta V_{PV} \cdot 100}{V_{PV-1Hz}}$ (per cent)								
	V_{PH} (m s^{-1})	2645	2876	2703	2910	2738	2955	2803	3020
		8,7		7,7		7,9		7,7	
	$\frac{\Delta V_{PH} \cdot 100}{V_{PH-1Hz}}$ (per cent)								
	V_{SV} (m s^{-1})	1546	1550	1525	1602	1526	1638	1620	1671
	V_{SH} (m s^{-1})	1723	1880	1745	1901	1752	1919	1773	1933
Pierre shale $S_w \approx 70$ per cent	V_{PV} (m s^{-1})	2265	2790	2330	2866	2343	2919	2356	2975
		23,2		23,0		24,6		26,3	
	$\frac{\Delta V_{PV} \cdot 100}{V_{PV-1Hz}}$ (per cent)								
	V_{PH} (m s^{-1})	2787	3342	2844	3343	2826	3358	2822	3395
		19,9		17,6		18,8		20,3	
	$\frac{\Delta V_{PH} \cdot 100}{V_{PH-1Hz}}$ (per cent)								
	V_{SV} (m s^{-1})	1163	1636	1187	1670	1269	1670	1494	1714
	V_{SH} (m s^{-1})	1332	1993	1401	1978	1495	1968	1625	1996

Table 6. List of *P*-wave velocity stress-sensitivity and strain-sensitivity factors obtained during isotropic loading of as-received Mancos shale and differently saturated Pierre shale I core plugs.

		S_{PV} (per cent MPa^{-1})	R_{PV} (−)	S_{PH} (per cent MPa^{-1})	R_{PH} (−)
Mancos shale	1 Hz	0,24	40	0,54	165
	Ultrasonic	0,10	16	0,24	56
Pierre shale I $S_w \approx 10$ per cent	1 Hz	0,82	31	0,32	25
	Ultrasonic	0,63	24	0,14	11
Pierre shale I $S_w \approx 23$ per cent	1 Hz	0,71	30	0,28	–
	Ultrasonic	0,69	29	0,69	–
Pierre shale I $S_w \approx 48$ per cent	1 Hz	0,71	29	0,40	35
	Ultrasonic	0,74	31	0,33	30
Pierre shale I $S_w \approx 70$ per cent	1 Hz	0,27	21	0,08	–
	Ultrasonic	0,44	34	0,11	–

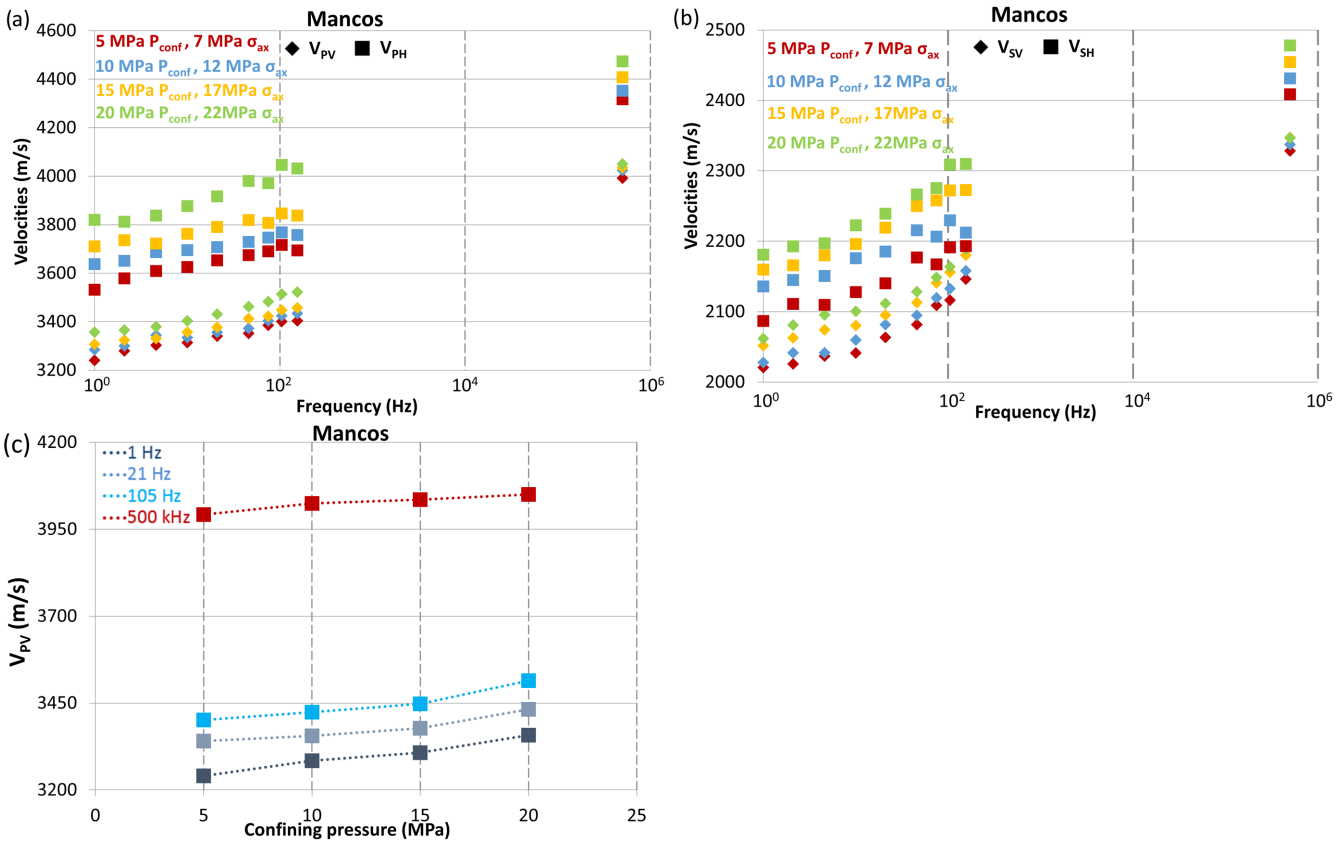

Figure 9. Seismic and ultrasonic directional *P*- and *S*-wave velocities of as-received Mancos shale as a function of frequency (a,b) and stress sensitivity of vertical *P*-wave velocity (c).

5 DISCUSSION

The most important finding of the present work is the frequency dependent stress sensitivity of elastic wave velocities of Pierre shale and Mancos shale. The frequency dependence is more pronounced for Mancos shale than for Pierre shale. Because of relatively large experimental uncertainties, further studies would have to be performed before final conclusions can be drawn. However, the present data obtained with Mancos shale, indicate that the stress sensitivity of velocities might be significantly higher at seismic frequencies than at ultrasonic frequencies (by up to a factor 2.5). This is an important finding since if one would attempt to invert time-lapse seismic data for the subsurface stress changes based on the ultrasonic laboratory measurements with core plugs, then in case of Mancos shale, ignoring the frequency dependence of the stress sensitivity could result in a large overestimation of the stress changes. In addition, ultrasonic laboratory measurements are sometimes carried out as part of screening studies for 4-D seismic. By ignoring the frequency dependence of the stress sensitivity, in case of Mancos shale, one might come to the conclusion that time-lapse time shifts for the expected stress changes in the field would be too small to be detected, while in reality, time shifts could well be above the detection limit because of an enhanced stress sensitivity at seismic frequencies. For Pierre shale, the frequency dependence of the stress sensitivity of velocities is smaller but would still have to be taken into account when comparing stress dependent measurements at seismic and ultrasonic frequencies. To this end however, it is important to note that the stress

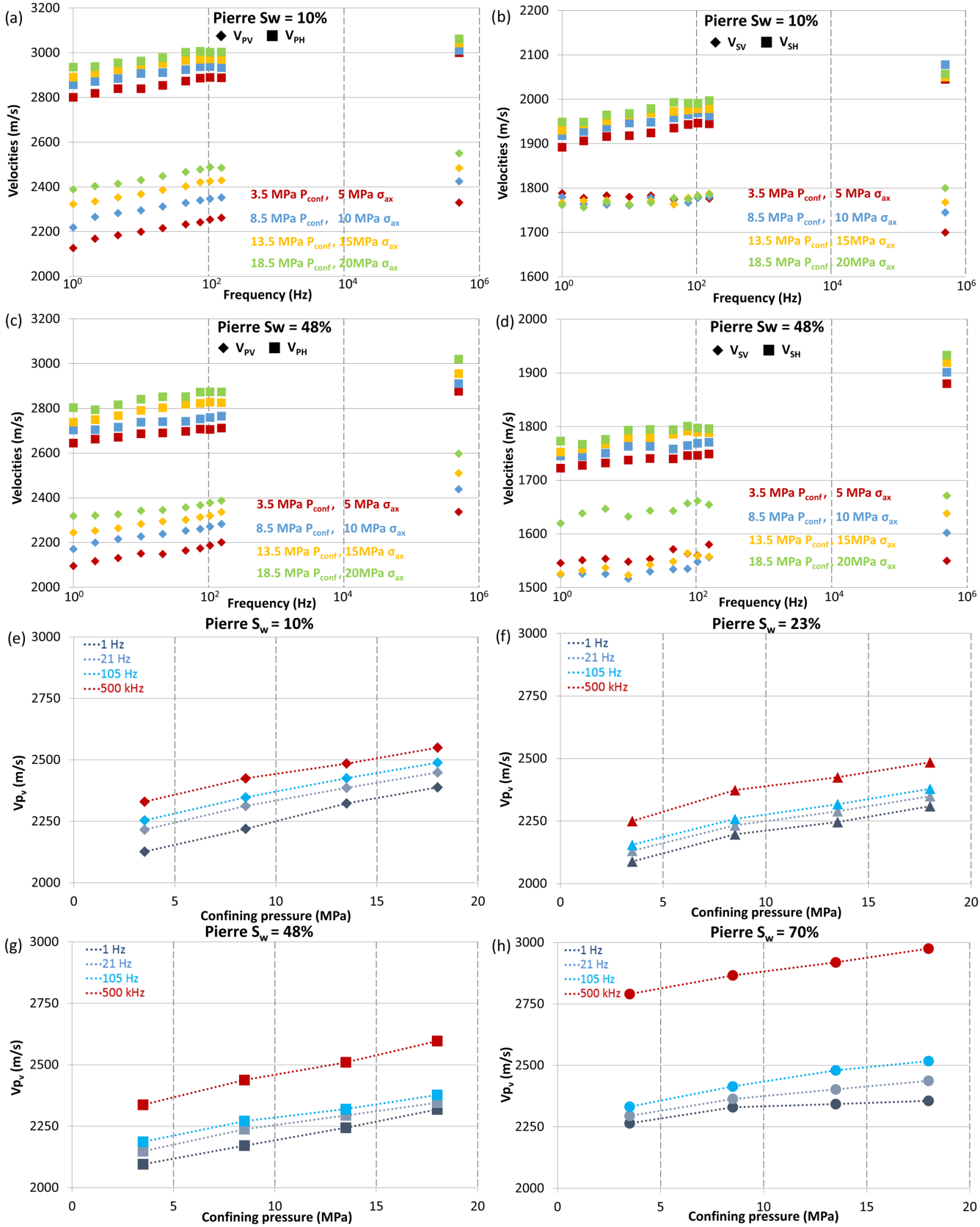

Figure 10. Seismic and ultrasonic directional *P*- and *S*-wave velocities of partially saturated Pierre shale I as a function of frequency (a–d) and stress sensitivity of vertical *P*-wave velocity (e–h).

sensitivity of velocities is dependent on the degree of water saturation, and also the frequency dependence of the stress sensitivity seems to be affected by water saturation. As demonstrated for highly saturated Pierre shale samples, for some cases the stress sensitivity may be higher at ultrasonic frequencies.

Another interesting result of this paper is the highly anisotropic stress sensitivity of studied shales. Moreover, the Young's modulus and elastic wave velocities of the Mancos shale loaded parallel to the bedding (90° sample) exhibits higher stress-sensitivity then in case of sample loaded perpendicular to the bedding (0° core plug), and the value of ε increases with stress, which is rather surprising and counterintuitive. The cracks being present in the rocks are most likely oriented with their normals perpendicular to the bedding planes, and thus while closing with stress, the ε should decrease while 0° samples should exhibit higher stress-sensitivity. The presented data were obtained with core plugs drilled from single batch of material, and ε was determined based on measurements performed with two different samples, therefore due to the experimental uncertainties, the tests should be repeated before the final conclusions could be drawn. This being said, the stress-sensitivity of Mancos shale Young's moduli changes very consistently with a drilling angle (almost no stress-sensitivity for 0° samples, 45° core plugs exhibit higher stress-sensitivity, 90° samples shows the highest stress-sensitivity), and changes are above the predicted errors. Further theoretical analysis is needed to understand those data, however they could indicate that the stress applied to the 0° sample did not stiffen it completely, whereas it was high enough to stiffen 90° core plugs. Assuming that the crack models can be applied for shales, stiff material (90° samples) are more likely to show higher sensitivity to weak planes or cracks than weak rocks (0° samples) that did not stiffen up due to external stress. In addition, higher stress sensitivity for samples loaded parallel to the bedding was observed in some cases during previous in house ultrasonic tests with Mancos shale (mostly at low confinement), although in most cases S_{PV} and S_{PH} were not too different. Our experience also show, that if the sample deviates from TI symmetry, such effects may be interpreted, which may indicate slight misalignment of sample orientation with the bedding plane (although eq. 21 was preserved). The increase of ε with stress could be on the other hand understood by the re-alignment of the anisotropic minerals (increase of the intrinsic anisotropy), that overcome the reduction of the anisotropy due to crack closure. However, whether the clay platelets are able to realign within the time scale of a laboratory experiment is an ongoing debate and remain to be proven. For Mancos shale, also data showing the dispersion of the independent elements of stiffness tensor, where the highest dispersion is observed for C_{11}, are debatable. In general, under assumption that the crack induced local flow mechanisms are responsible for dispersion in shales, one might have expected larger dispersion for C_{33}. However, based on number of our tests in which differently saturated core plugs were exposed to the same stress (Szewczyk *et al.* 2018), we believe that the dispersion in Mancos and Pierre shales is mainly dictated by the squirt-flow type mechanisms operating on a grain scale level (similar conclusions for clay containing rocks can be made based on ultrasonic measurements shown in Marketos & Best 2010) and that larger features like cracks plays a secondary role. Provided that the majority of cracks have their normals oriented perpendicular to the bedding, slightly higher dispersion observed for C_{11} could indirectly contribute to this hypothesis. For Pierre shale, similar anisotropy of the stress-sensitivity as shown in this work, was reported before by Ong *et al.* (2016) for calcareous shale, where anisotropic hydrostatic stress-sensitivity of ultrasonic velocities and a large decrease of the Thomsen's parameters at low confining stresses, was observed. Based on scanning electron microscope images, Ong *et al.* (2016) identified 'crack-like' pores with small aspect ratios, primarily oriented parallel to the bedding, as the most likely factor governing both directional and pressure dependencies of shale properties.

A drawback of the technique applied in the present study to determine seismic dispersion is that, for anisotropic media such as shales with TI symmetry, measurements with three samples are needed to determine all 5 independent stiffness parameters and to compare the measurements at seismic and ultrasonic frequencies. Reduction of the experimental errors requires either homogeneous rocks or rocks with a distinct bedding orientation. Alternatively, errors could be reduced significantly if the *P*-wave modulus and shear modulus could directly be measured at seismic frequencies (e.g. Jackson *et al.* 1984; Jackson & Paterson 1993; Suarez-Rivera *et al.* 2001). These moduli are directly related to *P*- and *S*-wave velocities, which would make it possible to measure seismic and ultrasonic velocities with one core plug only. It should also be noted that samples were conditioned in the desiccators under room conditions prior to the experiments, and that the exposure of samples to different RH under stress (within the pressure vessel), could result in different rock property changes than reported in this manuscript (including possible different final saturation levels and stress sensitivities). Also, use of the different method for changing the saturation of samples could affect the final results of this paper. The exposure of shales to different RH does not give the well-defined saturations, this method is also affected by the saturation hysteresis and is not fully reversible. On the other hand, as argued by others (e.g. Schmitt *et al.* 1994), it is one of the least invasive methods, and if compared to the other available methods (drainage/imbibition) it allows obtaining more homogenous distribution of the fluid phase, due to elimination of the capillary artefacts.

The reason for a frequency dependence of the stress sensitivity of elastic waves is not fully understood yet. As demonstrated here however, it may be attributed to a stress-induced change in dispersion: an increase in effective stress (here, we only look at isotropic stresses and stresses well below the rock strength) results in the closure of cracks, stiffening of grain contacts, a reduction of porosity, and thus an increase in rock stiffness and elastic wave velocities (e.g. Todd & Simmons 1972; Chritensen & Wang 1985; Best & Sams 1997; Prasad & Manghnani 1997; Siggins & Dewhurst 2003; Best *et al.* 2007; Sarout & Gueguen 2008). As discussed in more detail elsewhere (Szewczyk *et al.* 2018), and in accordance with previous findings (Marketos & Best 2010), we believe that dispersion in shales is caused (at least partly) by a squirt-flow type mechanism at grain contacts or micro-cracks involving adsorbed (bound) water. With increasing stress, but also with decreasing water saturation, the soft pores are being compressed and the amount of adsorbed water at grain contacts diminishes, thus changing the flow and resulting in less dispersion. In addition, Mavko & Vanorio (2010) based on the squirt flow mechanism argued that the effective stress coefficient changes with frequency. All this could explain why generally a higher stress sensitivity is found for seismic frequencies than

for ultrasonic frequencies. To first order approximation, we may write the stress sensitivity of elastic wave velocities, $\frac{\Delta V(f)}{V(f)\cdot\Delta\sigma}$, as a sum of a stress sensitivity at the low-frequency limit, $(\frac{\Delta V(f)}{\Delta\cdot\sigma})_{f=0} = \frac{\Delta V_0}{\Delta\sigma}$, and the derivative of the dispersion with respect to stress:

$$\frac{\Delta V(f)}{V(f)\cdot\Delta\sigma} = \frac{1}{V(f)}\left[\frac{\Delta V_0}{\Delta\sigma} + \frac{\Delta V(f) - \Delta V_0}{\Delta\sigma}\right], \tag{24}$$

with $V(f)$ the velocity at a given frequency, f, V_0 the low frequency limit of the velocity, and σ the hydrostatic effective stress. If the water saturation increases, the shale softens due to decreasing capillary pressure and increased water adsorption at the grain contacts, and dispersion increases (Szewczyk *et al.* 2018). Therefore, we could expect that the second term on the right side of eq. (24) is increasing in amplitude, and since it is negative, it causes the stress sensitivity of *P*-wave velocities of Pierre shales to decrease with increasing saturation.

6 CONCLUSIONS

The stress and frequency dependence of the elastic stiffness and elastic wave velocities of partially saturated Mancos shale and Pierre shale I was investigated by combining dynamic-stiffness measurements at seismic frequencies and ultrasonic velocity measurements performed with sets of differently oriented core plugs. The experimental data confirms that both shales are highly dispersive and strongly anisotropic materials. Recorded dispersions of some of the shale properties were as high as 50 per cent between seismic and ultrasonic frequencies and direction dependant. We found that for both shale types, the stress sensitivity of velocities was frequency dependant, which was linked to stress-dependent dispersion. The frequency dependence of the stress sensitivity of *P*- and *S*-wave velocities is relevant for the interpretation of time-lapse seismic data and it has to be taken into account when deriving rock-physics models based on ultrasonic laboratory measurements for the description of stress-induced changes of seismic velocities.

ACKNOWLEDGEMENTS

This publication has been produced with support from the BIGCCS Centre, performed under the Norwegian research program Centres for Environment-friendly Energy Research (FME). The authors acknowledge the following partners for their contributions: ConocoPhillips, Gassco, Shell, Statoil, TOTAL, ENGIE and the Research Council of Norway (193816/S60). The authors would also like to acknowledge financial support from The Research Council of Norway, BP Norge, Dong, Engie, Maersk and Total through the KPN-project 'Shale Rock Physics: Improved seismic monitoring for increased recovery' at SINTEF Petroleum Research.

REFERENCES

Barkved, O.I. & Kristiansen, T., 2005. Seismic time-lapse effects and stress changes: examples from a compacting reservoir, *Leading Edge,* **24**(12), 1244–1249.

Batzle, M., Hofmann, R., Han, D. & Castagna, J., 2001. Fluids and frequency dependent seismic velocity of rocks, *Leading Edge,* **20**(2), 168–171.

Batzle, M., Hofmann, R. & Han, D., 2006. Heavy oils—seismic properties, *Leading Edge,* **25**(6), 750–757.

Bauer, A., Szewczyk, D., Hedegaard, J. & Holt, R.M., 2015. Seismic dispersion in Mancos shale, in *3rd International Workshop on Rock Physics*. Available at: http://3iwrp.org/submissions/abstracts/AB_DS20141212-RAD4FB44.pdf.

Best, A.I. & Sams, M.S., 1997. Compressional wave velocity and attenuation at ultrasonic and sonic frequencies in near-surface sedimentary rocks, *Geophys. Prospect.,* **45**(2), 327–344.

Best, A.I., Sothcott, J. & McCann, C., 2007. A laboratory study of seismic velocity and attenuation anisotropy in near-surface sedimentary rocks, *Geophys. Prospect.,* **55**(5), 609–625.

Biot, M.A., 1956. Theory of propagation of elastic waves in a fluid-saturated porous solid. I. Low-frequency range, *J. acoust. Soc. Am.,* **28**(2), 168–178.

Chapman, M., 2003. Frequency-dependent anisotropy due to meso-scale fractures in the presence of equant porosity, *Geophys. Prospect.,* **51**(5), 369–379.

Chapman, M., Liu, E. & Li, X-Y., 2006. The influence of fluid-sensitive dispersion and attenuation on AVO analysis, *Geophys. J. Int.,* **167**(1), 89–105.

Chenevert, M.E. & Amanullah, M., 1997. Shale preservation and testing techniques for borehole stability studies, in *Proceedings of the 1997 SPE/IADC Drilling Conference,* Amsterdam, The Netherlands, pp. 863–868.

Christensen, N.I. & Wang, H.F., 1985. The influence of pore and confining pressure on dynamic elastic properties of Berea Sandstone, *Geophysics,* **50**(2), 207–213.

Cole, K.S. & Cole, R.H., 1941. Dispersion and absorption in dielectrics—I. Alternating current characteristics, *J. Chem. Phys.,* **9**(4), 341–352.

Deng, J., Wang, S. & Han, D.H., 2009. The velocity and attenuation anisotropy of shale at ultrasonic frequency, *J. Geophys. Eng.,* **6**(3), 269–278.

Dewhurst, D.N. & Siggins, A.F., 2006. Impact of fabric, microcracks and stress field on shale anisotropy, *Geophys. J. Int.,* **165**(1), 135–148.

Dewhurst, D.N., Siggins, A.F., Sarout, J., Raven, M.D. & Nordgård-Bolås, H.M., 2011. Geomechanical and ultrasonic characterization of a Norwegian Sea shale, *Geophysics,* **76**(3), WA101–WA111.

Domnesteanu, P., McCann, C. & Sothcott, J., 2002. Velocity anisotropy and attenuation of shale in under- and overpressured conditions, *Geophys. Prospect.,* **50**(5), 487–503.

Duranti, L., Ewy, R. & Hofmann, R., 2005. Dispersive and attenuative nature of shales: multiscale and multifrequency observations, in *2005 SEG Annual Meeting,* Houston, USA, Expanded Abstracts, 1577.

Dvorkin, J. & Nur, A., 1993. Dynamic poroelasticity: a unified model with the squirt and the Biot mechanisms, *Geophysics,* **58**(4), 524–533.

Greenspan, L., 1977. Humidity fixed points of binary saturated aqueous solutions, *J. Res. Natl. Bur. Stand.,* **81**(1), 89–96.

Gueguen, Y. & Sarout, J., 2011. Characteristics of anisotropy and dispersion in cracked medium, *Tectonophysics,* **503**(1), 165–172.

Gurevich, B. & Lopatnikov, S.L., 1995. Velocity and attenuation of elastic waves in finely layered porous rocks, *Geophys. J. Int.,* **121**(3), 933–947.

Gurevich, B., Makarynska, D., de Paula, O.B. & Pervukhina, M., 2010. A simple model for squirt-flow dispersion and attenuation in fluid-saturated granular rocks, *Geophysics,* **75**(6), N109–N120.

Hatchell, P. & Bourne, S., 2005. Rocks under strain: strain-induced time lapse shifts are observed for depleting reservoirs, *Leading Edge,* **24**(12), 1222–1225.

Helbig, K., 1994. *Foundations of Anisotropy for Exploration Seismics,* 1st edn, Pergamon Press.

Holt, R.M., Nes, O.M., Stenebråten, J.F. & Fjær, E., 2012. Static vs. dynamic behavior of shale, in *46th US Rock Mechanics / Geomechanics Symposium,* Chicago, USA, ARMA-2015-542.

Holt, R.M., Bauer, A., Fjaer, E., Stenebråten, J.F., Szewczyk, D. & Horsrud, P., 2015. Relating static and dynamic mechanical anisotropies of shale, in *49th U.S. Rock Mechanics/Geomechanics Symposium,* San Francisco, USA, ARMA-2015-484.

Holt, R.M., Bauer, A., Bakk, A. & Szewczyk, D., 2016. Stress-path dependence of ultrasonic and seismic velocities in shale, in *86th SEG Annual Meeting,* Dallas, USA, Expanded Abstracts, pp. 3159–3163.

Hornby, B.E., 1998. Experimental laboratory determination of the dynamic elastic properties of wet, drained shales, *J. geophys. Res.,* **103**(B12), 29 945–29 964.

Jackson, I. & Paterson, M.S., 1993. A high-pressure, high-temperature apparatus for studies of seismic wave dispersion and attenuation, *Pure appl. Geophys.,* **141**(2), 445–466.

Jackson, I., Paterson, M.S., Niesler, H. & Waterford, R.M., 1984. Rock anelasticity measurements at high pressure, low strain amplitude and seismic frequency, *Geophys. Res. Lett.,* **11**(12), 1235–1238.

Johnston, D., 1987. Physical properties of shale at temperature and pressure, *Geophysics,* **52**(10), 1391–1401.

Johnston, J.E. & Christensen, N.I., 1995. Seismic anisotropy of shales, *J. geophys. Res.,* **100**(B4), 5991–6003.

Jones, L.E.A. & Wang, H.F., 1981. Ultrasonic velocities in Cretaceous shales from the Williston basin, *Geophysics,* **46**(3), 288–297.

Kaarsberg, E.A., 1959. Introductory studies of natural and artificial argillaceous aggregates by sound-propagation and X-ray diffraction methods, *J. Geol.,* **67**(4), 447–472.

Keller, L.M., 2017. Porosity anisotropy of Opalinus Clay: implications for the poroelastic behaviour, *Geophys. J. Int.,* **208**(3), 1443–1448.

Kellogg, H.E., 1977. Geology and petroleum of the Mancos B formation Douglas Creek Arch area, Colorado and Utah, in *Exploration Frontiers of the Central and Southern Rockies,* pp. 167–179, ed. Veal, H.K., Rocky Mountain Association of Geologists.

Kenter, C.J., Van den Beukel, A.C., Hatchell, P.J., Maron, K.P., Molenaar, M.M. & Stammeijer, J.G.F., 2004. Geomechanics and 4D: Evaluation of reservoir characteristics from time shifts in the overburden, in *Gulf Rocks 2004, the 6th North America Rock Mechanics Symposium (NARMS),* American Rock Mechanics Association.

Lucet, N. & Zinszner, B., 2006. Frequency dependence of velocity in carbonate rocks, in *SEG Technical Program Expanded Abstracts 2006,* Society of Exploration Geophysicists, pp. 1898–1902.

Marketos, G. & Best, A.I., 2010. Application of the BISQ model to clay squirt flow in reservoir sandstones, *J. geophys. Res.,* **115,** B06209, doi:10.1029/2009JB006495.

Mavko, G. & Jizba, D., 1991. Estimating grain-scale fluid effects on velocity dispersion in rocks, *Geophysics,* **56**(12), 1940–1949.

Mavko, G. & Nur, A., 1979. Wave attenuation in partially saturated rocks, *Geophysics,* **44**(2), 161–178.

Mavko, G. & Vanorio, T., 2010. The influence of pore fluids and frequency on apparent effective stress behavior of seismic velocities, *Geophysics,* **75**(1), N1–N7.

Mavko, G., Mukerji, T. & Dvorkin, J., 2009. *The Rock Physics Handbook,* 2nd edn, Cambridge Univ. Press.

McCann, C., Sothcott, J. & Best, A.I., 2014. A new laboratory technique for determining the compressional wave properties of marine sediments at sonic frequencies and in situ pressures, *Geophys. Prospect.,* **62**(1), 97–116.

Mikhaltsevitch, V., Lebedev, M. & Gurevich, B., 2014. A laboratory study of low-frequency wave dispersion and attenuation in water-saturated sandstones, *Leading Edge,* **33**(6), 616–622.

Mikhaltsevitch, V., Lebedev, M. & Gurevich, B., 2016. A laboratory study of the elastic anisotropy in the Mancos shale at seismic frequencies, in *SEG Technical Program Expanded Abstracts 2016,* pp. 3174–3178.

Morsy, S., Sheng, J.J. & Ezewu, R.O., 2013. Potential of waterflooding in shale formations, in *2013 SPE Nigeria Annual International Conference and Exhibition,* Lagos, Nigeria, SPE-167510.

Muller, T.M. & Gurevich, B., 2006. Effective hydraulic conductivity and diffusivity of randomly heterogeneous porous solids with compressible constituents, *Appl. Physics. Lett.,* **88**(12), 121924.

Muller, T.M., Gurevich, B. & Lebedev, M., 2010. Seismic wave attenuation and dispersion resulting from wave-induced flow in porous rocks—a review, *Geophysics,* **75**(5), 75A147–75A164.

Nakagawa, S., Kneafsey, T.J., Daley, T.M., Freifeld, B.M. & Rees, E.V., 2013. Laboratory seismic monitoring of supercritical CO_2 flooding in sandstone cores using the Split Hopkinson Resonant Bar technique with concurrent X-ray Computed Tomography imaging, *Geophys. Prospect.,* **61**(2), 254–269.

Nur, A. & Byerlee, J.D., 1971. An exact effective stress law for elastic deformation of rocks with fluids, *J. geophys. Res.,* **76**(26), 6414–6419.

Nye, J.F., 1985. *Physical Properties of Crystals: Their Representation by Tensors and Matrices,* Oxford Univ. Press.

Olgaard, D.L., Nuesch, R. & Urai, J., 1995. Consolidation of water saturated shales at great depth under drained conditions, in *Proceedings 8th Congress of the International Society for Rock Mechanics,* Tokyo, Japan, pp. 25–29.

Ong, O.N., Schmitt, D.R., Kofman, R.S. & Haug, K., 2016. Static and dynamic pressure sensitivity anisotropy of a calcareous shale, *Geophys. Prospect.,* **64**(4), 875–897.

Piane, C.D., Sarout, J., Madonna, C., Saenger, E.H., Dewurst, D.N & Raven, M., 2014. Frequency-dependent seismic attenuation in shales: experimental results and theoretical analysis, *Geophys. J. Int.,* **198**(1), 504–515.

Pimienta, L., Fortin, J. & Guéguen, Y., 2015. Bulk modulus dispersion and attenuation in sandstones, *Geophysics,* **80**(2), D111–D127.

Prasad, M. & Manghnani, M.H., 1997. Effects of pore and differential pressure on compressional wave velocity and quality factor in Berea and Michigan Sandstones, *Geophysics,* **62**(4), 1163–1176.

Pride, S.R. & Berryman, J.G., 2003a. Linear dynamics of double-porosity and dual-permeability materials. I. Governing equations and acoustic attenuation, *Phys. Rev. E,* **68**(3), 036603.

Pride, S.R. & Berryman, J.G., 2003b. Linear dynamics of double-porosity and dual-permeability materials. II. Fluid transport equations, *Phys. Rev. E,* **68**(3), 036604.

Priest, J.A., Best, A.I. & Clayton, C.R., 2005. A laboratory investigation into the seismic velocities of methane gas hydrate-bearing sand, *J. geophys. Res.,* **110,** B04102, doi:10.1029/2004JB003259.

Røste, T., Stovas, A. & Landrø, M., 2006. Estimation of layer thickness and velocity changes using 4D prestack seismic data, *Geophysics,* **71**(6), S219–S234.

Sarker, R. & Batzle, M., 2010. Anisotropic elastic moduli of the Mancos B shale- an experimental study, in *86th SEG Annual Meeting,* Denver, USA, Expanded Abstracts, pp. 2600–2605.

Sarout, J. & Guéguen, Y., 2008. Anisotropy of elastic wave velocities in deformed shales: Part 2—Modeling results, *Geophysics,* **73**(5), D91–D103.

Sarout, J., Esteban, L., Piane, C.D., Maney, B & Dewhurst, D.N., 2014a. Elastic anisotropy of Opalinus Clay under variable saturation and triaxial stress, *Geophys. J. Int.,* **198**(3), 1662–1682.

Sarout, J., Piane, C.D., Nadri, D., Esteban, L. & Dewhurst, D.N., 2014b. A robust experimental determination of Thomsen's δ parameter, *Geophysics,* **80**(1), A19–A24.

Schmitt, L., Forsans, T. & Santarelli, F.J., 1994. Shale testing and capillary phenomena, *Int. J. Rock Mech. Min. Sci. Geomech. Abstr.,* **51**(5), 411–427.

Schultz, L.G., Tourtelot, H.A., Gill, J.R. & Boerngen, J.G., 1980. Composition and properties of the Pierre shale and equivalent rocks,

northern Great Plains region, U.S. Geological Survey Professional Paper, 1064–B.

Siggins, A.F. & Dewhurst, D.N., 2003. Saturation, pore pressure and effective stress from sandstone acoustic properties, *Geophys. Res. Lett.,* **30**(2), 1089–1092.

Spencer, J.W., 1981. Stress relaxations at low frequencies in fluid-saturated rocks: attenuation and modulus dispersion, *J. geophys. Res.,* **86**(B3), 1803–1812.

Suarez-Rivera, R., Willson, S., Nakagawa, S., Nes, O.M. & Liu, Z., 2001. Frequency scaling for evaluation of shale and mudstone properties from acoustic velocities, in *2001 AGU Fall Meeting Abstracts,* AGU, T32E–0924.

Szewczyk, D., Bauer, A. & Holt, R.M., 2016. A new laboratory apparatus for the measurement of seismic dispersion under deviatoric stress conditions, *Geophys. Prospect.,* **64**(4), 789–798.

Szewczyk, D., Bauer, A. & Holt, R.M., 2018. The impact of saturation on seismic dispersion in shales—laboratory measurements, *Geophysics,* **83**(1).

Thomsen, L., 1986. Weak elastic anisotropy, *Geophysics,* **51**(10), 1954–1966.

Todd, T. & Simmons, G., 1972. Effect of pore pressure on the velocity of compressional waves in low porosity rocks, *J. geophys. Res.,* **77**(20), 3731–3743.

Tisato, N. & Madonna, C., 2012. Attenuation at low seismic frequencies in partially saturated rocks: measurements and description of a new apparatus, *J. Appl. Geophys.,* **86,** 44–53.

Vernik, L. & Nur, A., 1992. Ultrasonic velocity and anisotropy of hydrocarbon source rocks, *Geophysics,* **57**(5), 727–735.

Voigt, W., 1928. *Lehrbuch der Kristallphysik (mit Ausschluss der Kristalloptik)*, B.G. Teubner.

Wang, Z., 2002. Seismic anisotropy in sedimentary rocks, part 2: laboratory data, *Geophysics,* **67**(5), 1423–1440.

White, J.E., Mihailova, N. & Lyakhovitsky, F., 1975. Low-frequency seismic waves in fluid-saturated layered rocks, *J. acoust. Soc. Am.,* **57**(S1), S30, doi:10.1121/1.1995164.

Winkler, K. & Nur, A., 1979. Pore fluids and seismic attenuation in rocks, *Geophys. Res. Lett.,* **6**(1), 1–4.

Zadler, B.J., Le Rousseau, J.H., Scales, J.A. & Smith, M.L., 2004. Resonant ultrasound spectroscopy: theory and application, *Geophys. J. Int.,* **156**(1), 154–169.

Zhao, J., Wang, S., Yin, H., Ma, X., Yan, X. & Li, Z., 2015. Multi-band direct laboratory measurement-based dispersion analysis on reservoir rocks, in *3rd International Workshop on Rock Physics,* Perth, Australia.

Zimmerman, R.W., 1991. *Compressibility of Sandstones,* 1st edn, Elsevier Science.